REPORT DOCUMENTATION PAGE

Form Approved OMB NO. 0704-0188

1. REPORT DATE (DD-MM-YYYY)	2. REPORT TYPE	3. DATES COVERED (From - To)
16-03-2016	Final Report	22-Dec-2014 - 21-Dec-2015

4. TITLE AND SUBTITLE

Final Report: Enhancing the Bandwidth Utilization in the Millimeter-Wave Band and to Modernize the Digital Signal Processing Laboratory at the California State University, Bakersfield

5a. CONTRACT NUMBER
W911NF-15-1-0033

5b. GRANT NUMBER

5c. PROGRAM ELEMENT NUMBER
106012

6. AUTHORS

Hani Mehrpouyan

5d. PROJECT NUMBER

5e. TASK NUMBER

5f. WORK UNIT NUMBER

7. PERFORMING ORGANIZATION NAMES AND ADDRESSES

California State University - Bakersfield
9001 Stockdale Hwy

Bakersfield, CA   93311 -1022

8. PERFORMING ORGANIZATION REPORT NUMBER

9. SPONSORING/MONITORING AGENCY NAME(S) AND ADDRESS (ES)

U.S. Army Research Office
P.O. Box 12211
Research Triangle Park, NC 27709-2211

10. SPONSOR/MONITOR'S ACRONYM(S)
ARO

11. SPONSOR/MONITOR'S REPORT NUMBER(S)
66363-EL-REP.14

12. DISTRIBUTION AVAILIBILITY STATEMENT

Approved for Public Release; Distribution Unlimited

13. SUPPLEMENTARY NOTES
The views, opinions and/or findings contained in this report are those of the author(s) and should not contrued as an official Department of the Army position, policy or decision, unless so designated by other documentation.

14. ABSTRACT

This report summarizes the outcomes of the project outlined ENHANCING THE BANDWIDTH UTILIZATION IN THE MILLIMETER-WAVE BAND AND MODERNIZING THE DIGITAL SIGNAL PROCESSING LABORATORY. Throughout this project we have made significant accomplishments on both advancing the state of the art on millimeter-wave communications by developing new transmission mechanism, network models, and channel characterizations.

15. SUBJECT TERMS

Millimeter-wave communications, signal processing, communications, hardware impairments, wireless communications, 5G

16. SECURITY CLASSIFICATION OF:			17. LIMITATION OF ABSTRACT	15. NUMBER OF PAGES	19a. NAME OF RESPONSIBLE PERSON
a. REPORT	b. ABSTRACT	c. THIS PAGE			Hani Mehrpouyan
UU	UU	UU	UU		19b. TELEPHONE NUMBER
					661-654-2837

Report Title

Final Report: Enhancing the Bandwidth Utilization in the Millimeter-Wave Band and to Modernize the Digital Signal Processing Laboratory at the California State University, Bakersfield

ABSTRACT

This report summarizes the outcomes of the project outlined ENHANCING THE BANDWIDTH UTILIZATION IN THE MILLIMETER-WAVE BAND AND MODERNIZING THE DIGITAL SIGNAL PROCESSING LABORATORY. Throughout this project we have made significant accomplishments on both advancing the state of the art on millimeter-wave communications by developing new transmission mechanism, network models, and channel characterizations.

Enter List of papers submitted or published that acknowledge ARO support from the start of the project to the date of this printing. List the papers, including journal references, in the following categories:

(a) Papers published in peer-reviewed journals (N/A for none)

Received		Paper
08/27/2015	1.00	Hani Mehrpouyan, Michail Matthaiou, Rui Wang, George K. Karagiannidis. Hybrid Millimeter-Wave Systems: A Novel Paradigm for HetNets, IEEE Communications Magazine, (01 2015): 216. doi:
TOTAL:	**1**	

Number of Papers published in peer-reviewed journals:

(b) Papers published in non-peer-reviewed journals (N/A for none)

Received	Paper
TOTAL:	

Number of Papers published in non peer-reviewed journals:

(c) Presentations

Number of Presentations: 0.00

Non Peer-Reviewed Conference Proceeding publications (other than abstracts):

<u>Received</u>   <u>Paper</u>

TOTAL:

Number of Non Peer-Reviewed Conference Proceeding publications (other than abstracts):

Peer-Reviewed Conference Proceeding publications (other than abstracts):

<u>Received</u>   <u>Paper</u>

08/27/2015   2.00   Rui Wang, Hani Mehrpouyan, Meixia Tao, Yingbo Hua. Optimal training design and individual channel estimation for MIMO two-way relay systems in colored environment,
GLOBECOM 2014 - 2014 IEEE Global Communications Conference. 07-DEC-14, Austin, TX, USA. : ,

08/27/2015   6.00   Vida Vakilian, Hani Mehrpouyan, Yingbo Hua. High rate space-time codes for millimeter-wave systems with reconfigurable antennas,
2015 IEEE Wireless Communications and Networking Conference (WCNC). 08-MAR-15, New Orleans, LA. : ,

08/27/2015   7.00   Hani Mehrpouyan, Mahmoud Ahmadian, Mohammad Azarbad, Abbas Koohian. Bandwidth Efficient Channel Estimation for Full Duplex Communication Systems,
IEEE International Conference on Communications . 06-JUN-15, . : ,

TOTAL: **3**

Number of Peer-Reviewed Conference Proceeding publications (other than abstracts):

(d) Manuscripts

<u>Received</u>   <u>Paper</u>

03/16/2016 13.00 Weiyang Xu, Wei Xiang, Maged Elkashlan, Hani Mehrpouyan. Spectrum Sensing of OFDM Signals in the Presence of Carrier Frequency Offset,
IEEE Transactions on Vehicular Technology (10 2016)

03/16/2016 12.00 Wanchun Liu, Xiangyun Zhou, Salman Durrani, Hani Mehrpouyan, Steven D. Blostein. Energy Harvesting Wireless Sensor Networks: Delay Analysis Considering Energy Costs of Sensing and Transmission,
IEEE Transactions on Wireless Communications (10 2016)

03/16/2016 11.00 Abbas Koohian, Hani Mehrpouyan, Ali A. Nasir, Salman Durrani, Mohammad Azarbad, Steven D. Blostein. Blind Channel Estimation in Full Duplex Systems: Identifiability Analysis, Bounds, and Estimators,
IEEE Transactions on Signal Processing (10 2016)

08/27/2015 5.00 Hani Mehrpouyan, Yingbo Hua, Hamid Jafarkhani, Vida Vakilian. High-Rate Space Coding for Reconfigurable 2X2 Millimeter-Wave MIMO Systems,
IEEE Communications Letters (07 2015)

08/27/2015 4.00 Rui Wang, , Hani Mehrpouyan, , Mexia Tao, , Yingbo Hua. Channel Estimation, Carrier Recovery, and Data Detection in the Presence of Phase Noise in OFDM Relay Systems,
IEEE TRANSACTIONS ON Wireless Communications (02 2015)

08/27/2015 8.00 Solmaz Niknam, Hani Mehrpouyan, Ali A. Nasir. Resource Allocation for Multi-User Hybrid Millimeter-Wave HetNets,
IEEE Global Communication Conference (07 2015)

08/27/2015 9.00 Salman Durrani, David Matolak, Hani Mehrpouyan, Ali A. Nasir. Non-Coherent FSK: An Attractive Modulation Set for Millimeter-Wave Communications,
IEEE Global Communication Conference (07 2015)

   TOTAL: **7**

Number of Manuscripts:

Books

<u>Received</u>   <u>Book</u>

   TOTAL:

<u>Received</u>   <u>Book Chapter</u>

TOTAL:

Patents Submitted

Patents Awarded

Awards

A. NASA: Research Initiation Grant Program, $50,000, awarded, 2016-2017, PI.

B. National Science Foundation XPS: DSL for Enabling Parallelism in Communication System Analysis and Simulation $258,000, PI (under review).

C. National Institute of Standards and Technology: Enabling Millimeter-Wave Communications via Reconfigurable Antennas $402,000, PI (under review).

D. National Science Foundation CI-P: System Testbed for Hybrid Millimeter-Wave Photonic Interconnects $100,000, CO-PI (under review).

Graduate Students

<u>NAME</u>	<u>PERCENT_SUPPORTED</u>
FTE Equivalent:	
Total Number:	

Names of Post Doctorates

<u>NAME</u>	<u>PERCENT_SUPPORTED</u>
FTE Equivalent	
Total Number:	

Names of Faculty Supported

<u>NAME</u>	<u>PERCENT_SUPPORTED</u>
FTE Equivalent:	
Total Number:	

Names of Under Graduate students supported

NAME	PERCENT_SUPPORTED
FTE Equivalent:	
Total Number:	

Student Metrics
This section only applies to graduating undergraduates supported by this agreement in this reporting period

The number of undergraduates funded by this agreement who graduated during this period: 0.00

The number of undergraduates funded by this agreement who graduated during this period with a degree in science, mathematics, engineering, or technology fields:------ 0.00

The number of undergraduates funded by your agreement who graduated during this period and will continue to pursue a graduate or Ph.D. degree in science, mathematics, engineering, or technology fields:------ 0.00

Number of graduating undergraduates who achieved a 3.5 GPA to 4.0 (4.0 max scale):...... 0.00

Number of graduating undergraduates funded by a DoD funded Center of Excellence grant for Education, Research and Engineering:...... 0.00

The number of undergraduates funded by your agreement who graduated during this period and intend to work for the Department of Defense 0.00

The number of undergraduates funded by your agreement who graduated during this period and will receive scholarships or fellowships for further studies in science, mathematics, engineering or technology fields: 0.00

Names of Personnel receiving masters degrees

NAME
Total Number:

Names of personnel receiving PHDs

NAME
Total Number:

Names of other research staff

NAME	PERCENT_SUPPORTED
FTE Equivalent:	
Total Number:	

Sub Contractors (DD882)

Inventions (DD882)

Scientific Progress

See attachment.

Technology Transfer

Attended the ARL Research Open house and have had various fruitful interactions with researchers. We are planing to work on join projects now related to the field of millimeter-wave communicants.

ENHANCING THE BANDWIDTH UTILIZATION IN THE MILLIMETER-WAVE BAND AND MODERNIZING THE DIGITAL SIGNAL PROCESSING LABORATORY

by

Mehrpouyan, Hani

Progress Report Submitted to

Department of the Army

US Army Research, Development and Engineering Commans

Army Research Office

California State University, Bakersfield

Bakersfield, California

August of 2015

Contents

List of Figures

Chapter 1

Foreword

W IRELESS systems are increasingly supporting larger and more diverse applications, e.g., sensor networks for environmental monitoring, to "smart grid" electrical infrastructures, to advances in medicine and transportation. To meet these demands, 50 billion wireless devices will interconnect people and machines by 2020 [59]. Increasingly, bandwidth represents the largest capital expenditure by cellular providers, even though the spectrum in the $30 - 300$ GHz, i.e., the millimeter-wave (mm-wave) band, is underutilized. Thus, to reliably meet the needs of a massive user base and to offer potential gains to underserved audiences, we are exploring new technologies, e.g., hybrid heterogeneous networks and reconfigurable antennas, to overcome *channel sparsity*, *high pathloss*, and *significant shadowing* that have been barriers to mm-wave band use. Doing so can potentially have vast reaching effects ranging from more *affordable* cellular access, to better *coverage* in remote areas, to supporting new services.

Moreover, this project has significantly upgraded the facilities at the Department of Electrical and Computer Engineering and Computer Science at California State University Bakersfield (CSUB) by enabling the PI to acquire various testing

and measurement equipment that can be used to enhance instructional, research, and outreach activities at this university.

Chapter 2

Statement of the Problems Studied

2.1 Design of Hybrid Wireless Networks using V- and E-band Spectrums

To more effectively share the network resources, wireless networks have adopted the widely accepted notion of *heterogeneous networks (HetNets)*, see Fig. 2.1. By employing smaller and more specialized cells, such networks can more efficiently meet the user's needs and improve the overall throughput of cellular networks [3, 18,23,41,63,65]. However, the close vicinity of many users and cellular BSs and the interference amongst these devices in HetNets, has introduced new challenges to the design of communication systems. Although many algorithms and approaches have been proposed for interference management and alignment in HetNets [28, 58], these schemes are mainly complex in nature and may not be suitable for cost and power sensitive wireless applications.

A more revolutionary approach to enhancing the throughput of next generation
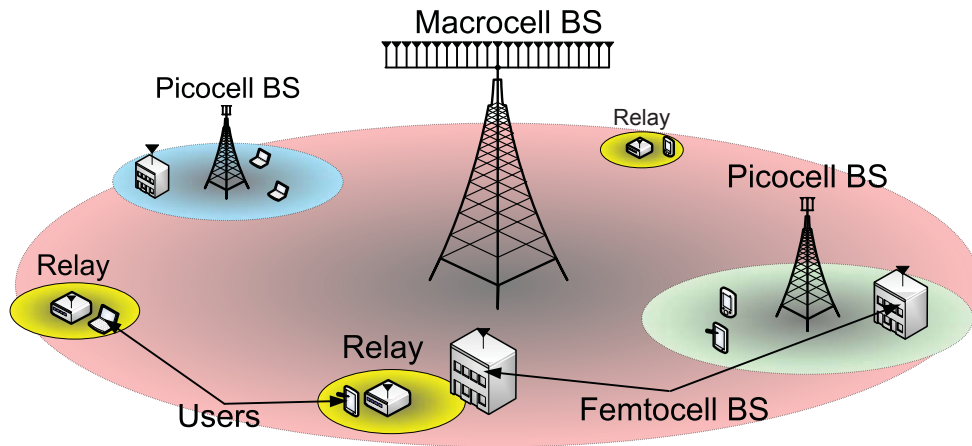
Figure 2.1: A HetNet with a macrocell BS and multiple supporting picocell BSs, femtocells, and relays.

HetNets is to take advantage of the large available *unlicensed* spectrum in the V-band [46, 51]. In addition, the high radio signal attenuation factor and high antenna directivity in the V-band ensures that V-band based HetNets do not suffer from significant interference [25, 62]. However, these characteristics, which are beneficial from an interference management point-of-view, can also limit V-band systems ability to meet the quality of service (QoS) and throughput requirements of users in cellular networks. Thus, new and innovative solutions are needed to circumvent the shortcomings of V-band systems and enable the wide deployment of millimeter-wave based HetNets.

As shown in Fig. 2.2, compared to the V-band, the atmospheric absorption in the *licensed* E-band spectrum is much lower (approximately 16 dB lower). Moreover, the FCC regulations allow for higher transmission power in the E-band compared to the V-band (maximum transmit power of 0.5 W and 3 W for the V- and E-band,
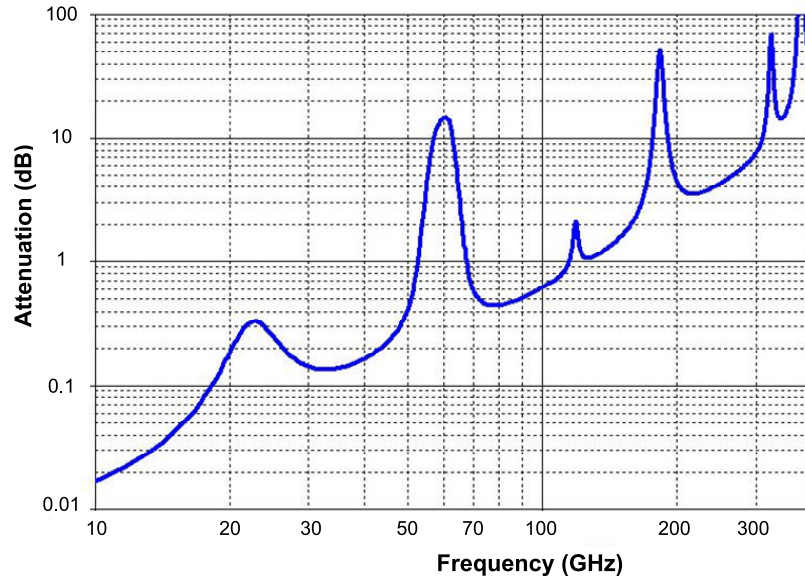
Figure 2.2: Atmospheric attenuation vs. frequency [62].

respectively) [62]. Thus, we propose to take advantage of the combined characteristics of V- and E-band systems, to reduce interference and enhance throughput and link availability in future millimeter-wave based HetNets. Specifically, we propose to apply the V-band to establish ultra-high-speed short-range links, while the E-band will be applied to establish the longer-range links and carry the backhaul between the HetNet BSs. In this proposal, this concept is denoted by *Hyrbid HetNets*. The research challenges for developing a framework for hybrid HetNets are outlined in the subsequent subsections.

To accomplish the above the following research problems need to be solved:

- Establish and develop an analytical framework for utilizing the V- or/and E-band spectrums to meet the link throughout requirements for hybrid HetNets while reducing interference.

5

- Developing algorithms for transition between V- and E-band communications for competing transceiver structures that represent a trade-off between performance and costs/complexity.

2.2 Addressing Channel Sparsity and High Pathloss in MIMO Millimeter-Wave Systems via Reconfigurable Antennas

Mm-wave communications mainly take place through *line-of-sight (LoS)* links to overcome the large signal attenuation in this band [50, 60] and to take advantage of the greater antenna directivity at these higher frequencies [25]. Moreover, MIMO systems combined with beamforming approaches are considered to further circumvent the pathloss and shadowing issues at mm-wave frequencies [30, 52, 66]. However, there is more to address, as even with the above adjustments, the resulting LoS MIMO channels are known to be sparse [4, 67]. This is because LoS MIMO systems can only achieve full-rank channels when the transmitter and receiver distance and the antenna spacings are set to specific optimal values [5]. As shown in *Fig. 2.3*, deviations from this optimal spacing (denoted by η) can result in significant performance degradation. One frequently explored solution among today's researchers is to use a large array of antennas in the mm-wave band to obtain gains similar to those of small *none line-of-sight (NLoS)* MIMO systems that take advantage of rich scattering [67]. However, this approach can add complexity, costs, and potentially large loss issues [20]. A more applicable and fundamentally different approach is to use reconfigurable antennas and their various states to
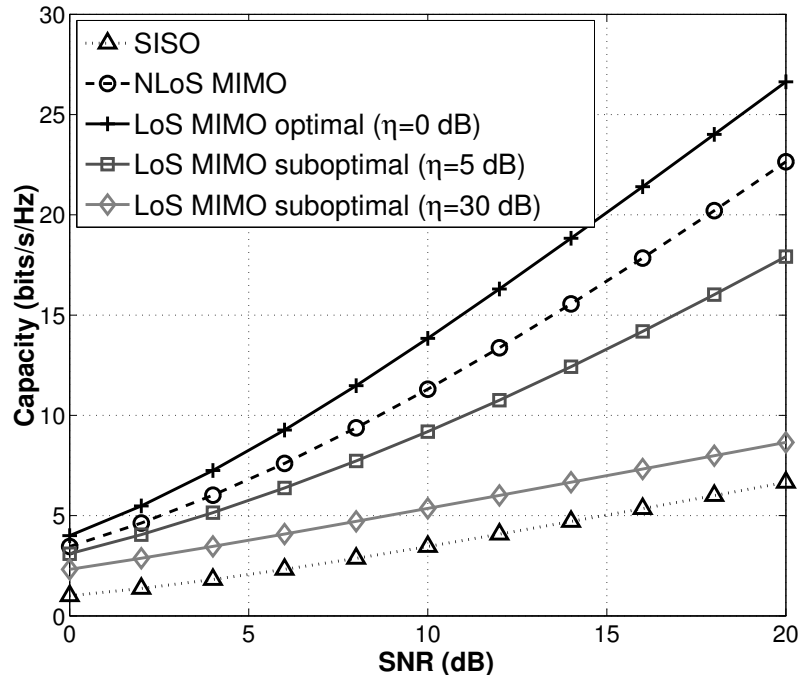
Figure 2.3: Capacity of a 4×4 MIMO system vs. the deviation with respect to optimal antenna spacing, i.e., $\eta \triangleq \frac{\text{Antenna Separation Product}_{\text{opt}}}{\text{Antenna Separation Product}}$.

modify the radiation pattern of *each* element of the MIMO array and to eliminate the dependency on the optimal antenna and transceiver spacing.

Traditional antennas cannot modify their radiation pattern and frequency of operation. Hence, a new class of antennas termed, *reconfigurable antennas*—which can dynamically change their radiation characteristics—have been the subject of intensive research [2, 10, 11, 14, 17, 19, 47, 48]. Researchers have reported several reconfigurable antennas architectures that can provide radiation pattern diversity [12, 27, 31, 71]. This diversity allows for the radiation pattern from each transmit-to-receive antenna pair in a MIMO system to be adjusted to ensure the LoS MIMO channel is full-rank, irrespective of the transceiver and antenna spacing. *Fig. 2.4* illustrates the proposed concept and compares it with beamforming for traditional
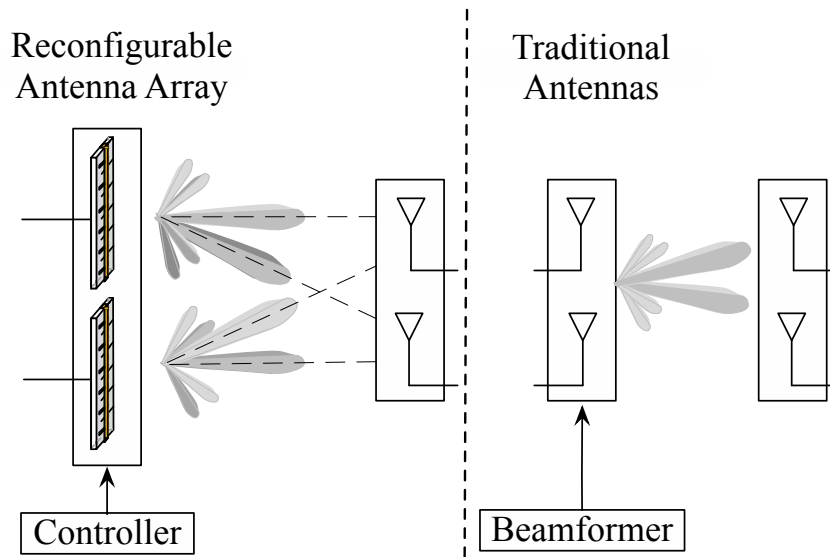
Figure 2.4: A 2×2 MIMO system equipped with reconfigurable antennas can form **four** main radiation lobes, while one equipped with conventional antennas can at most form **two** main radiation lobes via beamforming.

antennas [35, 74]. Reconfigurable antennas that can produce independent main lobes as shown in *Fig. 2.4* are available for commercial applications, e.g., leaky-wave antennas [8, 32–34, 37, 49]. It is also noteworthy that the reconfigurability of the radiation pattern and frequency of operation can increase the antenna gain and allow for operations over a wider frequency range, respectively. These are both desirable at mm-wave frequencies [50, 61]. In fact, aside from the PI's preliminary work [69, 70], there are very few results to date that utilize the degrees of freedom provided by reconfigurable antennas to address channel sparsity in MIMO mm-wave systems.

Instead of using the more commonly applied massive MIMO systems to overcome challenges in opening up mm-wave frequencies, we propose to use a small number of reconfigurable antennas. This approach is likely less costly and more

practical to implement. Reconfigurable antennas have various states that result in different radiation characteristics and patterns. These states provide a MIMO system with more degrees of freedom that can be used to design new beamforming and precoding algorithms to overcome channel sparsity, high path loss, and significant shadowing at mm-wave frequencies. This is very much an open research area with outcomes that can be applied to many interesting and important problems, and whose solutions offer potentially far-reaching effects.

2.3   Non-Coherent FSK: An Attractive Modulation Set for Millimeter-Wave Communications

It is anticipated that 5G cellular networks will support a significantly larger set of applications compared to 4G. These applications span sensor networks, the smart grid, the medical field, and vehicular communications [59]. Moreover, it is expected that 50 billion wireless devices will be deployed by 2020 [59]. A large portion of these devices will support machine-to-machine communications, e.g., autonomous vehicles. Hence, next generation cellular networks have to support a significantly larger number of users. To meet this demand on higher data capacity and higher data rates, 5G networks must take advantage of the frequencies in the millimeter-wave (mm-wave) band, i.e., 30–300 GHz [50, 59]. It is important to mention that current standards, e.g., Wireless Gigabit Alliance (WiGig) and IEEE 802.11ad operate over the unlicensed 60 GHz frequency band.

Given large bandwidth that is available for communications in the mm-wave band, the potential of mm-wave for establishing high speed communication links

is well-understood. However, there are significant hurdles that need to be over-
come before mm-wave communication systems can become mainstream. Some
of these issues are related to the high free-space pathloss and shadowing that is
present at mm-wave frequencies [42, 50]. In fact, for the same transmit power and
data rate, mm-wave communication systems are expected to be able to support
significantly shorter links when compared to wireless systems in the microwave
band [44, 72]. Moreover, mm-wave systems are affected by other impairments
such as amplifier non-linearity and phase noise that stem from the extremely high
frequencies that the RF transceivers need to operate at [26, 72]. Thus, significant ef-
forts are being made to address these issues through the use of massive multi-input
multi-output systems (MIMO) [57], sophisticated relaying approaches [40], physi-
cal layer designs that are robust to amplifier non-linearity [64], and estimation and
synchronization algorithms that mitigate the impact of phase noise [43, 45].

Although the above approaches are extremely effective at overcoming the afore-
mentioned challenges at the mm-wave band, they add further complexity to the
transceiver structures, which are already prohibitively high due to utilization of
a very large bandwidth. The authors believe that simple solutions that can over-
come the propagation and hardware impairments issues at this band may be bet-
ter suited to utilize the vast bandwidth at mm-wave frequencies. As such, here,
we focus on utilizing non-coherent frequency shift keying (FSK) for circumvent-
ing the challenges at mm-wave frequencies. Moreover, since current standards,
e.g., WiGig and IEEE 802.11ad, support both single carrier modulation and multi-
carrier orthogonal frequency division multiplexing (OFDM), we choose to use sin-
gle carrier modulation to avoid extreme sensitivity of OFDM to amplifier non-
linearity [64].

Rationale for proposing use of FSK: Due to the scarcity of bandwidth in the microwave band, non-coherent FSK has been mainly pushed to the sidelines in today's cellular networks. The M-ary non-coherent FSK utilizes a larger bandwidth as the size of the constellation, M, increases [54]. For example, a system utilizing 4 quadrature amplitude modulation (QAM) and achieving a data rate of 2 Gbps, requires 1 GHz of bandwidth. On the other hand, it can be easily calculated that a system using 4-ary non-coherent FSK and achieving the same data rate as above needs 4 times as much bandwidth or 4 GHz to be exact. However, unlike QAM or phase shift keying (PSK), where as the order of modulation set, M, increases the bit error rate (BER) of the system also increases, the BER of M-ary non-coherent FSK decreases with an increasing M [54]. Thus, M-FSK can use the large bandwidth at mm-wave frequencies* to achieve multi Gbps wireless links, while also improving the BER performance of the system. The latter can help overcome the issues associated with pathloss and shadowing in this band. In other words, we are indicating that it is beneficial to sacrifice bandwidth efficiency to achieve higher data rates and better BER performance using M-FSK since there is such an abundance of untapped bandwidth that is available at mm-wave frequencies.

The remainder of this paper also shows that M-FSK has other desirable properties that make it even more suitable for mm-wave applications. In fact, via extensive simulations we show that M-FSK is extremely robust to both phase noise and amplifier non-linearity. However, a survey of literature shows that non-coherent FSK has been mainly overlooked for applications in this band. Application of M-FSK in the mm-wave band has been briefly discussed in [26]. However, there are

---

*From 57–64 GHz, 71–76 GHz, and 81–86 GHz. Moreover, there is even more bandwidth available that is still unlicensed including 120–180 GHz and 200–300 GHz.

11

no discussions on the impact of phase noise and amplifier non-linearity on the performance of M-FSK. In [6], the authors briefly demonstrate the potential of FSK achieving high data rates in indoor environment at the mm-wave frequencies. However, again there are no investigations related to the effect of hardware impairments on the performance of M-FSK. The phase noise parameters for system using M-FSK has been analyzed in [1]. However, there are no performance evaluation on the actual effect of phase noise on the BER performance of M-FSK.

In this section, we demonstrate via simulations that non-coherent FSK can utilize the vast bandwidth at mm-wave frequencies to combat significant pathloss and shadowing in this band, while being robust to amplifier non-linearity and phase noise. To support our findings, we establish a comprehensive simulation setup and set of parameters that consider the impact of pathloss, shadowing, amplifier non-linearity, and phase noise, at the 60 GHz band. Our results indicate that non-coherent FSK outperforms phase shift keying, and quadrature amplitude modulation, at mm-wave frequencies. This outcome combined with the low detection complexity of non-coherent FSK make it an attractive modulation for achieving multi Gbps wireless links at mm-wave frequencies. Moreover, the proposed comprehensive simulation setup can be applied to investigate and validate the performance of various mm-wave systems in practical settings.

2.4 Modernizing the Digital Signal Processing Laboratory at CSUB

California State University, Bakersfield (CSUB) is categorized as a minority and Hispanic serving university that serves a large number of students in the Kern

County and southern California.[†] The School of Engineering at CSUB was officially launched in September of 2011. There are a total of 250 students that are enrolled in the Computer and Electrical Engineering Programs at the Department of Electrical and Computer Engineering and Computer Science (ECCS) and this number is expected to grow by an average of 10% year over year for the next three years. In order to ensure effective student training in the engineering discipline, there was a need for specialized hardware and software labs that could be used in areas such as signals and systems, signal processing, digital communications, wireless networks etc. Although the Digital Signal Processing and Communication Laboratory (DSPCL) at CSUB was equipped with basic testing and measurement equipment and could partially meet the above need, there was a lack of instrumentation for carrying out RF, microwave, and millimeter-wave analysis and testing in this lab. Thus, this funding opportunity has gone a long way in modernizing DSPCL and enhancing the training and research capabilities of the Department of ECCS at CSUB. Moreover, the Department of ECCS is heavily involved in community outreach programs, which are designed to attract local high school students to join STEM programs. These initiates ensure that the acquired equipment will be accessible to a larger audience including high school students and educators.

[†]It is noteworthy that there are no major universities within a hundred mile radius of CSUB.

Chapter 3

Summary of the Most Important Results

3.1   Resource Allocation for Hybrid HetNets

Building upon the work in [61], we propose a framework for an OFDM mm-wave hybrid HetNet that exploit the bandwidth and propagation characteristics at the *V-band*, and the *E-band*. To date, we have proposes a two-hop transmission scheme for mm-wave HetNets, see Fig. 3.1. The proposed HetNet uses relays to overcome the high pathloss and shadowing at mm-wave frequencies. A joint resource allocation is proposed for this setup. A new degree of freedom in which a subcarrier applied in the second hop might be different from the one used in the first hop, is also considered. This technique, which is called subcarrier pairing, improves the system sum-rate [22] and can be combined with frequency band selection to enhance *coverage* at mm-wave frequencies. For example, if a relay-to-user link distance is longer than that of the BS-to-relay link, and cannot be adequately supported via the V-band, subcarrier pairing allows for the use of an E-band subcarrier to support this link. Subsequently, the resource allocation problem for the proposed mm-wave HetNet is analytically formulated. The resulting optimization is then solved
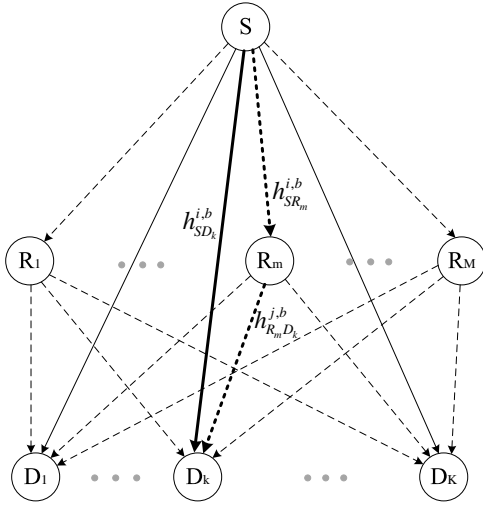
Figure 3.1: Downlink transmission in a single cell of the HetNet.
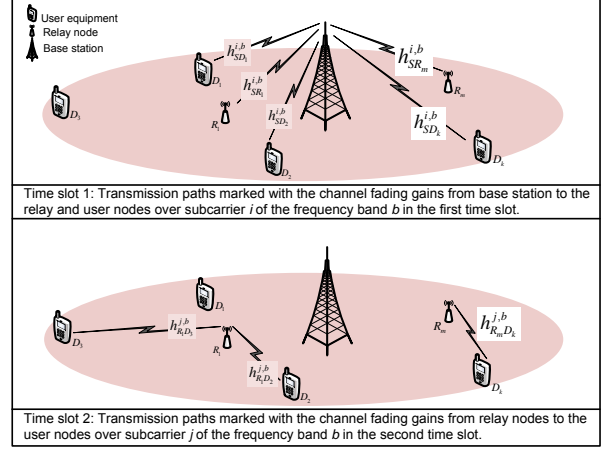
Figure 3.2: Timing diagram for transmission in direct link and relay modes.

via the dual decomposition approach. Finally, by using the sub-gradient method and an iterative algorithm, the joint resource allocation problem is solved. Simulations show that by using smaller cells, relays, and different *propagation* characteristics at both the V- and E-band, the proposed HetNets can overcome the large pathloss and shadowing at mm-wave frequencies and achieve significantly high date rates.

In the following we only present our simulation results to date and refer the reader to Appendix A for derivations for the resources allocation problem.

The simulation results that demonstrate the advantage of the proposed joint resource allocation problem in enhancing the overall sum-weighted-rate of mm-wave HetNets by utilizing the E- and V-band spectrums and their specific propagation characteristics, performing subcarrier pairing, relay selection, and power allocation. LoS of links are assumed given the high antenna directivity in the mm-wave band. Moreover, we consider the extended large-scale path-loss model,

15
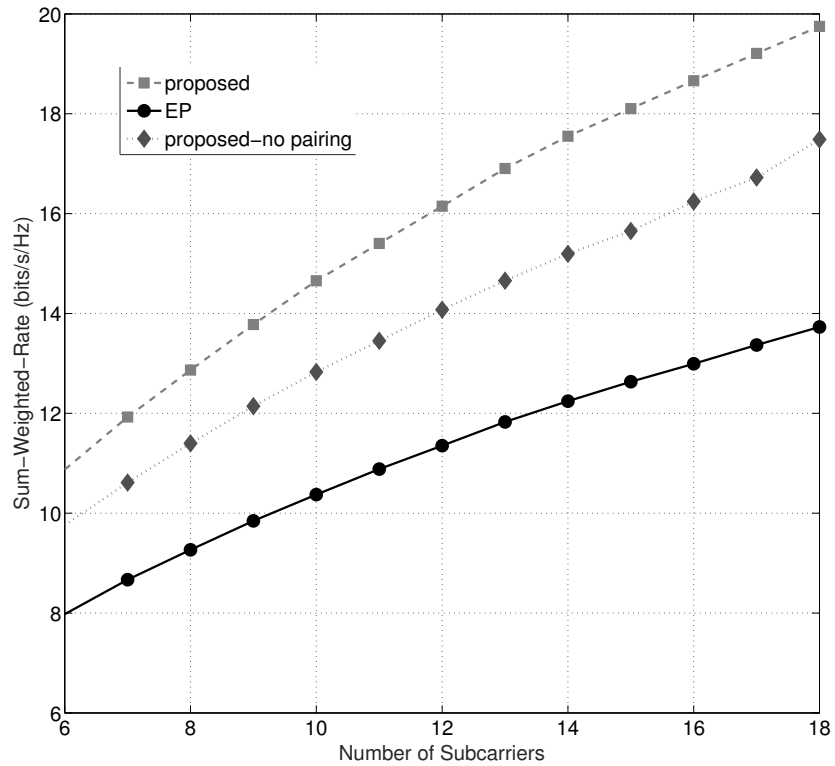
Figure 3.3: Sum-weighted-rate vs. number of subcarriers for $K = 6$, $M = 4$.

which is dependent on the distance and frequency of operation [50]. In order to model large-scale fading, the reference distance is set to be $d_0 = 5$ meter. The distance between the transmitter and receiver are 50 and 25 meters in the direct and relay links, respectively. We set the other large scale parameter, i.e., pathloss exponent to 1.7 and 0.7 for the 60 GHz and 70–80 GHz bands, respectively. Moreover, the shadowing effect of the channels is modeled by a zero-mean Gaussian random variable with standard deviation 1.8 dB and 4.8 dB for the 60 GHz and 70–80 GHz bands, respectively [50], [55]. The minimum rate requirement for the users is set to 3 (bits/sec/Hz) and the total transmit power is set to 8.4 dB.

In the proposed scheme, initial Lagrangian multipliers are randomly set and

the step size for the subgradient method is set to $0.5/\sqrt{l}$, where l denotes the iteration index. ε_δ and ε_τ are set to be 10^{-3}. The weights w_k are considered to be $w_k = 1 + (k-1)/(K-1), \forall k \in \{1, ..., K\}$ [24]. Three different schemes are considered:

- *Proposed*: The jointly resource allocation scheme presented.

- *EP*: The conventional equal power scheme in which no power allocation is applied, i.e., power is equally allocated to the subcarriers in both bands.

- *Proposed-no pairing*: The joint resource allocation proposed without subcarrier pairing, i.e., the subcarriers in the first and second time slots are the same.

The sum-weighted-rate of the network versus number of subcarriers for $K = 6$ users and $M = 4$ relays is shown in Fig. 3.3. As anticipated, it can be observed that by increasing the number of the subcarriers, the sum-weighted-rate of the network increases for all three schemes. However, the proposed joint resource allocation outperforms the other two schemes. Moreover, it can be observed that the biggest gain is obtained by applying power allocation while subcarrier pairing also provides reasonable gains.

In Fig. 3.4 the sum-weighted-rate of the three scenarios under consideration are versus the number of the users in the network with $M = 5$ relays and $N = 25$ subcarriers. Again we observe a similar pattern as that of Fig. 3.3, where power allocation provides the biggest gain followed by subcarrier pairing. This can be mainly attributed to the nature of mm-wave channels, which are significantly affected by shadowing and pathloss. Hence, power allocation provides a very effective approach to meet both propagation challenges. Moreover, subcarrier pairing
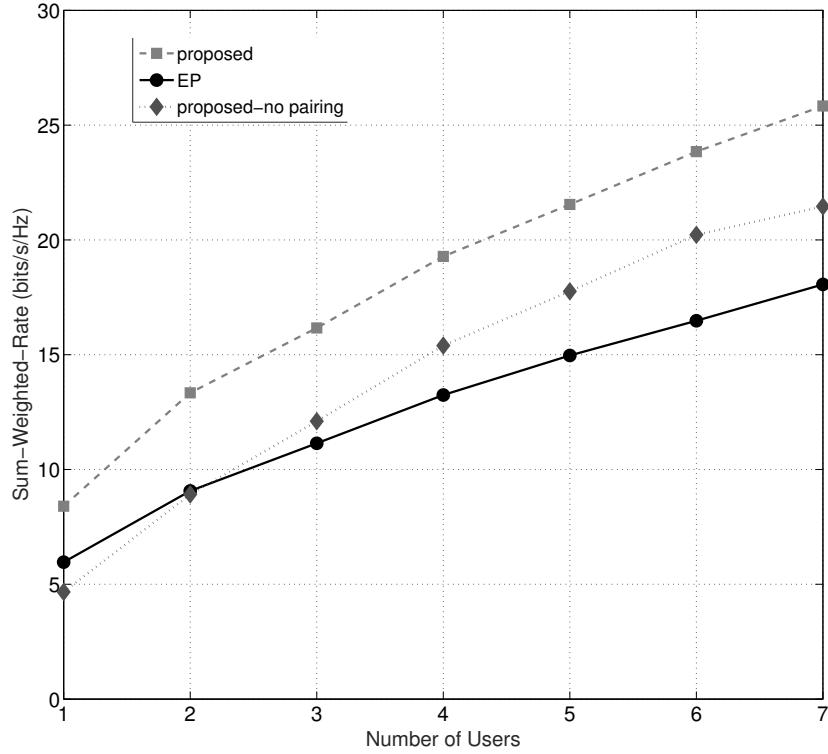
Figure 3.4: Sum-weighted-rate vs. number of users for $N = 25$, $M = 5$.

provides the resource allocation algorithm with the flexibility to switch between V- and E-band based on the channel conditions in both bands. This is the main reason that the proposed algorithm outperforms the approach with no subcarrier pairing in Figs. 3.3 and 3.4.

Fig. 3.5 depicts the sum-weighted-rate of the proposed HetNet when utilizing both V- and E-band and V-band versus the number of the subcarriers. Fig. 3.5 shows E-band can be effectively used to overcome the significant path loss at V-band frequencies. In fact, because of the strong signal attenuation in the V-band, communication over this band is only possible over short-range distances. Hence,
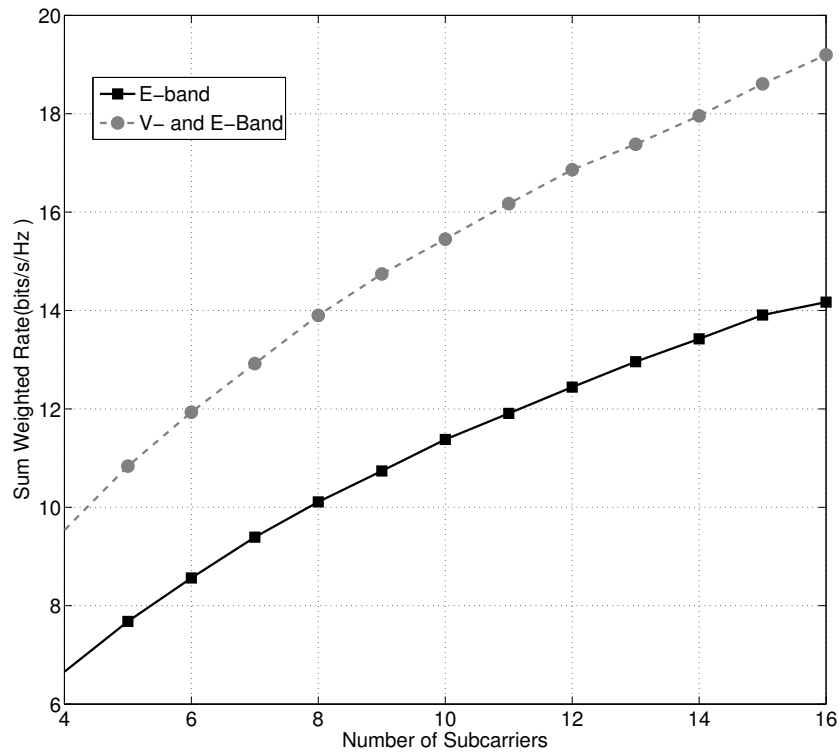
Figure 3.5: Sum-weighted-rate vs. number of subcarriers for $M = 3$, $K = 4$.

the users that are far from base station and/or the relays experience poorer received signal-to-noise ratios, which causes a reduction in their data rate accordingly. On the other hand, by also including E-band in the resource allocation problem, a HetNet can take advantage of the lower pathloss in the E-band to enhance the overall sum-weighted-rate of the network. Thus, Fig. 3.5 indicates the importance of utilizing various bands within the mm-wave band within future HetNets.
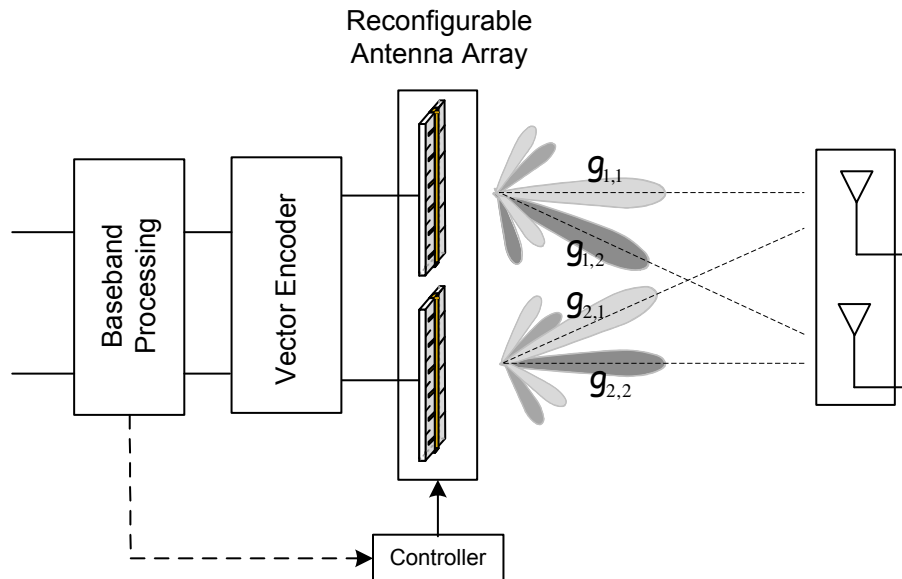
Figure 3.6: Reconfigurable MIMO system transmitter

3.2 Resolving Channel Sparsity in 2×2 MM-Wave MIMO Systems

Let us consider a MIMO system with $N_t = 2$ reconfigurable transmit antennas with controllable radiation patterns [9] and $M_R = 2$ receive antennas, see *Fig. 3.6*. Since mm-wave application are considered, the channel parameters are assumed to follow a Rician flat fading distribution [50, 60]. At this stage, the transmitter is assumed to have access to the complete CSI. The CSI can be obtained through feedback from the receiver (small MIMO system and limited feedback) or by assuming channel reciprocity and TDD operations [38]. To demonstrate the potential of reconfigurable antennas to address channel sparsity, it is further assumed that the reconfigurable antennas have an *infinite* number of states. As part of future research, we will look into extensions to FDD scenarios and also considering

a finite number of reconfigurable antenna states. Moreover, each reconfigurable antenna is assumed to have two main radiation lobes that are steerable independently. Such antennas are available for commercial applications, e.g., leaky-wave antennas [8, 32–34, 37, 49].

Based on the above assumptions, the received signal can be expressed as

$$\mathbf{y} = \mathbf{H}_g \mathbf{c} + \mathbf{z}, \tag{3.1}$$

where $\mathbf{c} = [c_1, c_2, \cdots, c_{N_t}]^T \in \mathbb{C}^{N_t \times 1}$ is the transmitted code vector, $\mathbf{z} \in \mathbb{C}^{M_R \times 1}$ is a zero-mean complex white Gaussian noise, and $\mathbf{H}_g \in \mathbb{C}^{M_R \times N_t}$ is the Hadamard product of the channel matrix $\mathbf{H}$ and the reconfigurable antenna parameter matrix $\mathbf{G}$, i.e., [68–70]

$$\mathbf{H}_g = \mathbf{H} \circ \mathbf{G}. \tag{3.2}$$

In (3.2), $\mathbf{H} \triangleq [\mathbf{h}_1, \cdots, \mathbf{h}_{N_t}]$ with $\mathbf{h}_j \triangleq [h_{1,j}, \cdots, h_{M_R,j}]^T$, and $\mathbf{G} \triangleq [\mathbf{g}_1, \cdots, \mathbf{g}_{N_t}]$ with $\mathbf{g}_j \triangleq [g_{1,j}, \cdots, g_{M_R,j}]^T$. Here, $h_{i,j}$ denotes the channel parameters corresponding to the ith and jth receive and transmit antennas, respectively. Moreover, the antenna parameters, $\mathbf{G}$, are a one-to-one mapping from the antenna states to the antenna radiation patterns. Here, $g_{i,j}$ denotes the gain and radiation angle of the ith reconfigurable antenna that is pointed towards the jth receive antenna (see *Fig. 3.6*) [68–70]. The parameters $\mathbf{G}$ are modified by selecting a different state of the reconfigurable antenna, which result in a different radiation pattern. Since it is assumed that there are two main radiation lobes from each transmit antenna that are directed towards each receive antenna, a Hadamard product instead of a matrix product appears in (3.2). **This gives reconfigurable antennas more degrees of freedom and is the main difference between traditional beamforming and reconfigurable antenna beamforming.**
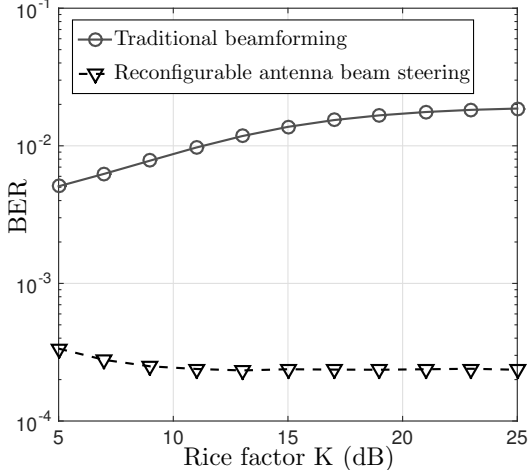
Figure 3.7: BER performance compari-son versus K, the Rician factor, (SNR= 10 dB).
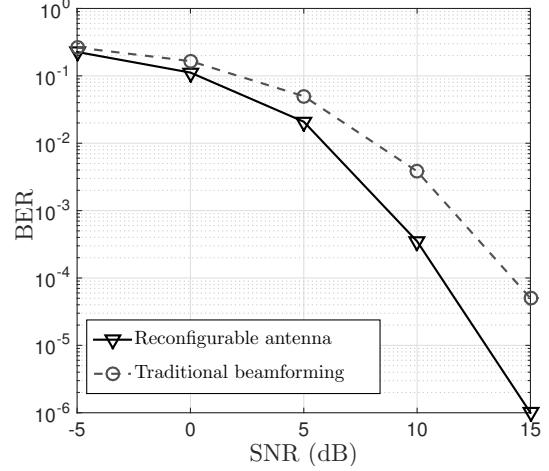
Figure 3.8: BER performance in Rician fading channels with $K = 2$ dB.

To achieve full diversity, the matrix $\mathbf{H}_g$ must be full-rank or equivalently its determinant must be nonzero. This condition may not be satisfied for MIMO mm-wave systems due to the LoS nature of the link. However, through beam steering by selecting different states of the reconfigurable antenna, one can ensure that the determinant of $\mathbf{H}_g$ is nonzero. Accordingly, to achieve full-rank channels, the op-timal antenna parameters at the transmitter, for $i, j = \{1, 2\}$, are given by

$$g_{1,j} = h_{1,j}^*/(|h_{1,1}|^2 + |h_{1,2}|^2), \quad g_{2,j} = (-1)^j h_{2,j}^*/(|h_{2,1}|^2 + |h_{2,2}|^2). \tag{3.3}$$

Due to the choice of reconfigurable antenna parameters in (3.3), the equivalent channel $\mathbf{H}_g$ is full-rank even when the channel matrix, $\mathbf{H}$, is not full-rank.

Fig. 3.7 demonstrates the advantage of using beam steering via reconfigurable antennas compared to beamforming with omnidirectional ones in Rician fading, i.e., $\mathbf{H} = \sqrt{\frac{K}{K+1}}\mathbf{H}_L + \sqrt{\frac{1}{K+1}}\mathbf{H}_w$, where K is the Rice factor. *Vertical Bell Laborato-ries Layered Space-Time Architecture (VBLAST)* is also used [16]. The random com-

22

ponent, $\mathbf{H}_w$, accounts for the scattered signals and its entries are modeled by a complex Gaussian random variable with mean zero and variance one. The deterministic component, $\mathbf{H}_L$, models the LoS channel according to [5] with $\eta = 10$ dB. As shown in this figure, traditional beamforming [74] cannot overcome channel sparsity. On the other hand, since a MIMO system using reconfigurable antennas and beam steering, as in (3.3), can maintain a full-rank channel, the system performance improves as the LoS component becomes stronger and the effect of fading is lessened. *Fig. 3.8* also supports the above outcome for a range of SNRs, which reaffirms the potential of the proposed method in addressing channel sparsity in mm-wave systems.

3.3 Non-Coherent FSK: An Attractive Modulation Set for Millimeter-Wave Communications

Suppose an information symbol $x_n \in \mathbb{C}$ is transmitted over a wireless narrowband channel $h \in \mathbb{C}$ with additive noise $\nu_n \in \mathbb{C}$, where n is the symbol index. In practice, physical radio-frequency (RF) transceivers suffer from hardware impairments such as phase noise, amplifier non-linearity, and IQ imbalance. The combined influence of these impairments can be modeled by a generalized channel model [40, 43], where the received signal is

$$y_n = e^{j\phi_n} h(x_n + \eta) + \nu_n, \tag{3.4}$$

Table 3.1: Range of values used for different simulation parameters [29, 36, 40, 50].

Simulation Parameters	Values
phase noise variance σ_{phn}^2	$\{10^{-4}, 10^{-3}, 10^{-2}, 10^{-1}\}$
hardware distortion noise variance σ_{nl}^2	$\{0.1, 0.2, 0.3\}$
shadowing-standard deviation σ_{shad}	$\{6, 7, \ldots, 12\}$ dB
pathloss exponent γ	$\{3, 3.5, \ldots, 5\}$

where ϕ_n corresponds to the nth sample of the phase noise and η is used to model the distortion noise that appear from the transceiver impairments, such as amplifier non-linearity and in-phase and quadrature-phase (IQ) imbalance. Additive noise ν_n is assumed to be white and complex Gaussian process with $\nu_n \sim \mathcal{CN}(0, N_o)$, $\forall\, n$, and N_o is the noise power per unit bandwidth. Based on [13, 15], the phase noise process can be modeled as a Brownian motion or Wiener process and is given by

$$\phi_n = \phi_{n-1} + \Delta_n \tag{3.5}$$

where the phase noise innovation Δ_n is assumed to be white real Gaussian process with $\Delta_n \sim \mathcal{N}(0, \sigma_{\text{phn}}^2)$ and σ_{phn}^2 is variance of the phase noise innovation process [43]. The distortion noise due to hardware impairments η, in (3.4), can be modeled as a complex Gaussian process with $\eta \sim \mathcal{CN}(0, \sigma_{\text{nl}}^2 P)$, where $P = \mathbb{E}_{x_n}\{|x_n|^2\}$ is the average power of the information symbols and σ_{nl}^2 is the hardware distortion noise variance.

In (3.4), we model the wireless channel h by [50]

$$h = \sqrt{\frac{K(f_c)}{\psi} \left(\frac{d_o}{d}\right)^{\gamma}} \left(\sqrt{\frac{K_R}{1+K_R}} h_{\text{LOS}} + \sqrt{\frac{1}{1+K_R}} h_{\text{NLOS}}\right), \quad (3.6)$$

where

- $K(f_c) \triangleq \left(\frac{\lambda}{4\pi d_o}\right)^2$, $\lambda = \frac{c}{f_c}$ is the wavelength of the carrier signal, c is the speed of light, f_c is the carrier frequency, d_o is the reference distance,

- ψ is log-normally distributed random variable which models the shadowing effect, such that μ_{shad} and σ_{shad} are the mean and standard deviation of the corresponding normally distributed random variable $10 \log_{10} \psi$,

- d is the distance between the transmitter and the receiver, γ is the path loss exponent,

- $h_{\text{LOS}} \triangleq e^{\frac{j2\pi a \sin\theta}{\lambda}}$ is the line-of-sight channel component, $a = \frac{\lambda}{2}$ is the antenna spacing, θ is the angle of arrival, $h_{\text{NLOS}} \sim \mathcal{CN}(0,1)$ is the complex normally distributed non-line of sight channel component, and the contribution of h_{LOS} and h_{NLOS} to the overall channel is denoted by the Rician factor K_R.

In (3.6), the factors $K(f_c)$, γ, and d correspond to the large scale fading while the factor $\sqrt{\frac{K_R}{1+K_R}} h_{\text{LOS}} + \sqrt{\frac{1}{1+K_R}} h_{\text{NLOS}}$ corresponds to the small scale fading in the wireless channel. Note that the model in (3.6) seems similar to the one used for microwave communication system, however mm-wave communication systems experience high levels of phase noise, amplifier non-linearity, shadowing, and pathloss [50]. The range of practical values for mm-wave systems are detailed in Table 3.1.

We propose to use *non-coherent frequency shift keying (FSK)* modulation where the phase of two different information symbols from the modulation set is not

necessarily be same and the signal is not continuous at bit transitions. The block diagrams for non-coherent FSK modulator and demodulator are given in [54]. Particularly, for orthogonality, the two frequencies from the modulation set must be integer multiple of $\frac{1}{2T_s}$ and their separation must be integer multiple of $\frac{1}{T_s}$, where T_s defines the symbol period. Though the bandwidth requirement for non-coherent FSK is large compared to other modulation schemes, such as phase shift keying (PSK) and quadrature amplitude modulation (QAM), however, we are targeting mm-wave communication where bandwidth is plentiful and is less of a concern. The main advantage of non-coherent FSK is its low detection complexity and as demonstrated in the following section through simulations, it can utilize the vast bandwidth at mm-wave frequencies to combat significant pathloss and shadowing in this band, while at the same time being robust to amplifier non-linearity and phase noise.

3.3.1   Simulation Setup for mm-Wave Systems

In this section, we present a simulation setup for mm-wave systems that considers pathloss, shadowing, amplifier non-linearity, and phase noise. The simulation setup described below can be applied to investigate and validate the performance of various mm-wave systems in practical settings. The range of values considered for the simulation parameters in our paper is given in Table 3.1 where the details with references is given below. Note that we consider broader range of values to also test the performance of non-coherent FSK over worst-case hardware impairment and channel distortion.

Phase Noise: The effect of phase noise is more profound at high frequencies in

mm-wave communication [42]. For the Si CMOS technology, it has been established in [29] that phase noise variance is $\sigma_{\text{phn}}^2 = 10^{-3}$ rad^2 at $f_c = 60$ GHz and system bandwidth $= 1$ MHz.[‡] Further, the phase noise variance increases by increasing the carrier frequency. In our simulation results, we investigate the effect of a range of phase noise variances $\sigma_{\text{phn}}^2 = \{10^{-4}, 10^{-3}, 10^{-2}, 10^{-1}\}$ on the system performance.

Amplifier non-linearity: The effect of hardware impairment, e.g., amplifier non-linearity is more severe at high frequencies in mm-wave communication [42]. Particularly, hardware distortion noise variance of $\sigma_{\text{nl}}^2 = 0.15$ is considered to be extremely high for microwave communication [40]. There is presently no amplifier non-linearity model, as the one presented in [40], for mm-wave systems. Hence, we investigate the effect of range of distortion noise variances $\sigma_{\text{nl}}^2 = \{0.1, 0.2, 0.3\}$ on the performance of different modulation schemes.

Shadowing: Empirical results and experiments, conducted for mm-wave communication systems in [56], establish that shadowing-standard deviation is $\sigma_{\text{shad}} = 9.13$ dB at 28 GHz. Considering the fact that we study the effect of channel distortions over a wide range of mm-wave frequencies 50-130 GHz, particularly over 60 GHz band, we consider the range of values of $\sigma_{\text{shad}} = \{6, 7, \ldots, 12\}$ dB to study the effect of shadowing on different modulation schemes.

Pathloss: The effect of pathloss is more significant at high frequencies in mm-wave communication due to atmospheric absorption [50]. It has been found through empirical results and experiments, conducted for mm-wave communication systems, that a signal transmitted from a 7 meter antenna height suffers from a path

---

[‡]Note that for constant bit rate of say 2 Mbps, the bandwidth required by non-coherent M-FSK will be M MHz and that required by M-PSK or M-QAM will be 1 MHz.
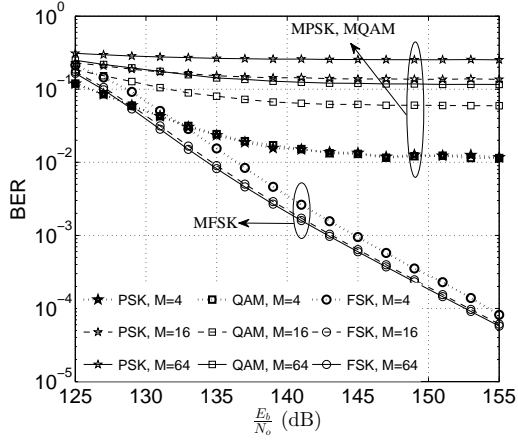
Figure 3.9: BER versus $\frac{E_b}{N_o}$ at the transmitter (reflects to $\frac{E_b}{N_o} = \{1, 6, \ldots, 31\}$ dB at the receiver) with phase noise variance $\sigma^2_{\text{phn}} = 10^{-3}$.
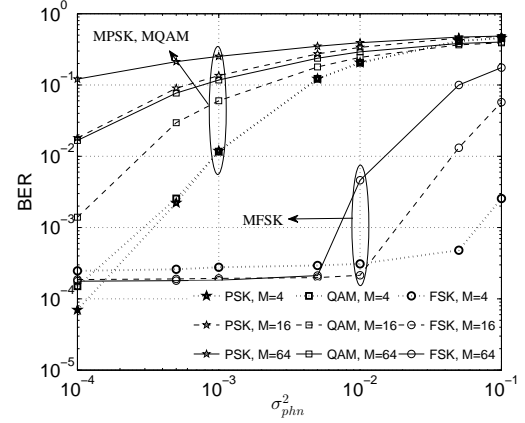
Figure 3.10: BER versus phase noise variance σ^2_{phn} at $\frac{E_b}{N_o} = 150$ dB at the transmitter (reflects to $\frac{E_b}{N_o} = 26$ dB at the receiver).

loss exponent of $\gamma = 3.73$ at 28 GHz [36]. In our results, we consider a range of values of path loss exponent, i.e,. $\gamma = \{3, 3.5, \ldots, 5\}$ to study its effect on different modulation schemes.

3.3.2 Simulations Results

In this section, the effect of hardware impairments and channel distortion on the performance of non-coherent FSK and different other modulation schemes, e.g., PSK and QAM, is studied through simulations. Particularly, we consider different modulation sizes, e.g., $M = \{4, 16, 64\}$ for non-coherent FSK, PSK, and QAM. To model small scale fading, we set the Rician factor $K_R = 5$ dB and the angle of arrival θ is a random number, i.e., uniformly distributed between 0 and 2π. To model large scale fading, we set the reference distance $d_o = 1$ meter and the distance between the transmitter and the receiver is set to $d = 25$ meters. Unless

otherwise stated, we set the other large scale fading parameters, i.e., path loss exponent $\gamma = 4$ and carrier frequency $f_c = 60$ GHz. The average symbol power $P = \mathbb{E}_{x_n}\{|x_n|^2\}$ is set to 1 and the noise power density N_o is set relative to bit energy E_b, i.e, we set $\frac{E_b}{N_o} = 150$ dB at the transmitter, unless stated otherwise. *Note that $\gamma 10 \log_{10} \frac{d}{d_o} - 10 \log_{10} K(f_c) = 124$ dB 'loss' is straightforwardly caused by the transmission at carrier frequency $f_c = 60$ GHz and with path loss exponent $\gamma = 4$ and $d = 25$ meters. Thus, $\frac{E_b}{N_o} = 150$ dB at the transmitter translates to the value of 26 dB at the receiver if the signal attenuation due to carrier frequency f_c and path loss exponent γ is ignored, as usually assumed in many papers.* It is further noteworthy that $\frac{E_b}{N_o} = 150$ dB is a practical value since typical base station transmits at a power of 46 dBm and typical noise density is -174 dBm/Hz. All results are averaged over 10^5 simulations with each simulation performed over a frame length of 100 symbols. The individual effect of phase noise, hardware distortion noise (due to IQ imbalance and amplifier non-linearity), shadowing, path loss exponent, and carrier frequency, over the range of values of these parameters, on the system performance is studied in the following sections (cf. Secs. 3.3.2.1-3.3.2.3). Finally, the combined effect of all the hardware impairments and channel distortions will be studied in Sec. 3.3.2.4.

3.3.2.1 Effect of Phase Noise

Fig. 3.9 plots the bit-error rate (BER) versus $\frac{E_b}{N_o}$ for a fixed value of phase noise variance $\sigma_{\text{phn}}^2 = 10^{-3}$ rad^2, while the effect of range of values of phase noise variance will be studied in Fig. 3.10. In Fig. 3.9, the range of values of $\frac{E_b}{N_o}$ in abscissa is between 125 and 155 dB. Again, note that if the signal attenuation of 124 dB caused by the transmission at carrier frequency $f_c = 60$ GHz and with path loss exponent $\gamma = 4$ and $d = 25$ meters, is ignored, $\frac{E_b}{N_o} = \{125, 130, \ldots, 155\}$ dB at the transmitter

will translate to the range $\{1, \ldots, 31\}$ dB at the receiver, which is usually considered in many papers.

It can be observed from Fig. 3.9 that the application of M-PSK and M-QAM fails to achieve the BER of less than 10^{-2}, even at $\frac{E_b}{N_o} = 155$ dB. As a matter of fact, the BER of a system employing M-PSK and M-QAM suffers from an error floor and the level of the error floor increases by increasing the modulation order M due to denser constellations. On the other hand, the application of M-FSK achieves a BER $< 1 \times 10^{-4}$ at $\frac{E_b}{N_o} = 155$ dB. In addition, the BER of a system employing M-FSK decreases by increasing the modulation order M at the cost of increased bandwidth. However, we are targeting mm-wave communication where bandwidth is plentiful and is less of a concern. Even if we assume modulation size of $M = 4$, for which 4-FSK requires only 4 times more bandwidth compared to that required by 4-PSK or 4-QAM, BER for 4-FSK is 100 times smaller than that for 4-PSK or 4-QAM at $\frac{E_b}{N_o} = 155$ dB. On the other hand, if we use $M = 64$ (taking advantage of the ample bandwidth in mm-wave band), 64-FSK not only achieves more than 200 times smaller BER but also delivers 4 times higher throughput (bits per second) when compared to 4-PSK or 4-QAM. It is important to mention that in the absence of phase noise, the effect of the modulation order M on the BER performance of M-PSK, M-QAM, and M-FSK follows the similar trend (increasing the modulation order M increases the BER for M-PSK and M-QAM and decreases the BER for M-FSK [54, page 522]) as the one that we have observed in the presence of phase noise $\sigma_{\text{phn}}^2 = 10^{-3}$.

In Fig. 3.10, we study the effect of range of values of phase noise variance on the BER performance at fixed value of $\frac{E_b}{N_o} = 150$ dB. It can be observed from Fig. 3.10 that M-FSK is capable of withstanding even severer phase noise, e.g.,
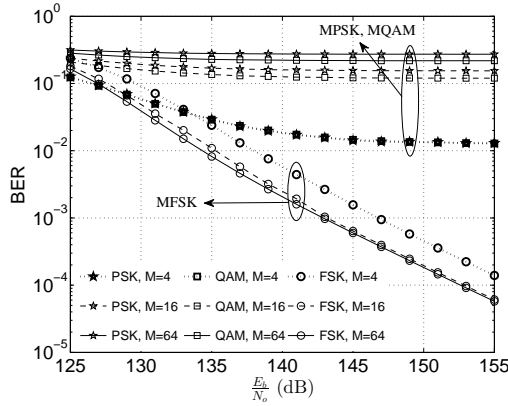
Figure 3.11: BER versus $\frac{E_b}{N_o}$ at the transmitter (reflects to $\frac{E_b}{N_o} = \{1, 6, \ldots, 31\}$ dB at the receiver) with hardware distortion noise variance $\sigma_{nl}^2 = 0.2$.
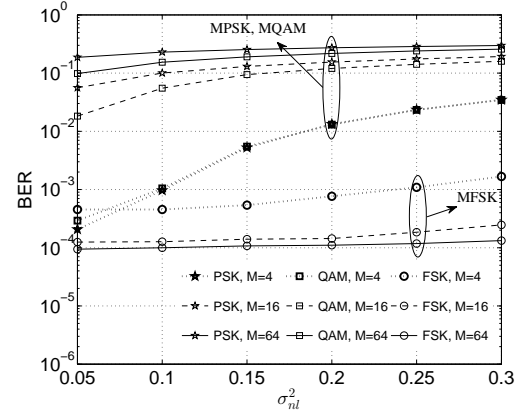
Figure 3.12: BER versus hardware distortion noise variance σ_{nl}^2 at $\frac{E_b}{N_o} = 150$ dB at the transmitter (reflects to $\frac{E_b}{N_o} = 26$ dB at the receiver).

$\sigma_{phn}^2 = 10^{-2}$ rad^2, where the application of M-PSK and M-QAM completely fails to help decode the received signal (BER $> 3 \times 10^{-1}$). Moreover, in case if phase noise gets extremely worse due to poor oscillators, e.g., $\sigma_{phn}^2 = 10^{-1}$ rad^2, employing 4-FSK can still achieve the BER $= 2.4 \times 10^{-3}$ where all other modulation schemes fails to recover the transmitted information. An important engineering insight is that the usual trend of M-FSK, i.e., increasing the modulation order M decreases the BER, is observed in the opposite way for strong values of phase noise variance $\sigma_{phn}^2 \geq 10^{-2}$ rad^2.

3.3.2.2 Effect of Other Hardware Distortions

In this subsection, we study the effect of other hardware distortions, such as amplifier non-linearity and IQ imbalance, modeled by η in (3.4), on the performance of different modulation schemes. Fig. 3.11 plots the bit-error rate (BER) versus $\frac{E_b}{N_o}$
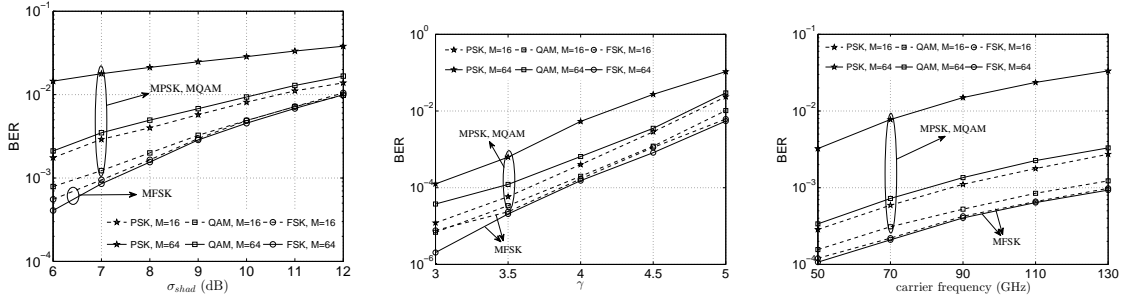
(a) shadowing standard deviation σ_{shad}

(b) path loss exponent γ

(c) carrier frequency f_c

Figure 3.13: BER versus (a) shadowing standard deviation σ_{shad}, (b) path loss exponent γ, and carrier frequency f_c, at $\frac{E_b}{N_o} = 150$ dB at the transmitter (reflects to $\frac{E_b}{N_o} = 26$ dB at the receiver).

for a fixed value of hardware distortion noise variance $\sigma_{\mathrm{nl}}^2 = 0.2$, while the effect of range of values of distortion noise variance will be studied shortly in Fig. 3.12. Similar to the case of phase noise as observed in Fig. 3.9, it can be observed from Fig. 3.11 that the presence of hardware impairments has a very destructive effect on the application of M-PSK and M-QAM, i.e., the BER suffers from an error floor and is greater than 10^{-2} even at $\frac{E_b}{N_o} = 155$ dB. On the other hand, employing M-FSK achieves the BER $< 1.3 \times 10^{-4}$ at $\frac{E_b}{N_o} = 155$ dB. As expected, increasing the modulation size from $M = 4$ to $M = 16$ or 64 decreases the BER of M-FSK-based system. Though, this is at the expense of increased bandwidth, but that does not matter much for mm-wave communication. It is noteworthy that for modulation size $M = 4$ and 64, BER for MFSK is about 100 and 3000 times, respectively, smaller than that for PSK or QAM at $\frac{E_b}{N_o} = 155$ dB.

In Fig. 3.12, we study the effect of range of values of hardware distortion noise variance on the BER performance at fixed value of $\frac{E_b}{N_o} = 150$ dB. It can be observed

from Fig. 3.10 that BER for M-FSK is smaller than 2×10^{-3} even against very strong effect of hardware impairment, e.g., $\sigma_{\mathrm{nl}}^2 = 0.3$, where the application of M-PSK and M-QAM may fail to recover the transmitted signal due to corresponding very high BERs. It is important to mention that BER performance for 64-FSK almost remains unaffected for the range of values of hardware distortion noise variance $\sigma_{\mathrm{nl}}^2 = (0.05, 0.3)$.

3.3.2.3   Effect of Large Scale Channel Fading

In this subsection, we will study the effect of large scale fading parameters, such as shadowing, path loss exponent, and carrier frequency, on the performance of different modulation schemes. Fig. 3.13 plots the BER versus shadowing-standard deviation σ_{shad} (Fig. 3.13(a)), (b) path loss exponent γ (Fig. 3.13(b)), and carrier frequency f_c (Fig. 3.13(c)), at $\frac{E_b}{N_o} = 150$ dB at the transmitter (which corresponds to 26 dB at the receiver). For clarity, the results are plotted only for modulation sizes $M = \{16, 64\}$. As expected, the BER performance for all modulation schemes gets worse by increasing shadowing-standard deviation σ_{shad}, path loss exponent γ, and carrier frequency f_c.

Fig. 3.13(a) displays the effect of shadowing on the system BER performance. We consider the range of values of $\sigma_{\mathrm{shad}} = \{6, 7, \ldots, 12\}$ dB to study the effect of shadowing on different modulation schemes. Fig. 3.13(a) shows that M-FSK offers smaller BER compared to M-PSK and M-QAM for the whole set of considered values of shadowing-standard deviation σ_{shad}. Particularly, for $\sigma_{\mathrm{shad}} = 9$ dB, 16-FSK achieves the BER $= 3 \times 10^{-3}$ which is 1.57 and 1.1 times smaller than that achieved by 16-PSK and 16-QAM, respectively. Similarly, 64-FSK achieves the BER $= 3 \times 10^{-3}$ which is 8.5 and 2.3 times smaller than that achieved by 64-PSK and

64-QAM, respectively.

Fig. 3.13(b) plots the effect of varying path loss exponent on the system BER performance. We consider the range of values of path loss exponent, i.e,. $\gamma = \{3, 3.5, \ldots, 5\}$ to study its effect on different modulation schemes. Fig. 3.13(b) shows that M-FSK offers smaller BER compared to M-PSK and M-QAM for the whole set of considered values of path loss exponent γ. Particularly, for $\gamma = 4$ dB, 16-FSK achieves the BER $= 1.7 \times 10^{-4}$ which is 2.3 and 1.2 times smaller than that achieved by 16-PSK and 16-QAM, respectively. Similarly, 64-FSK achieves the BER $= 1.5 \times 10^{-4}$ which is 35.3 and 4.3 times smaller than that achieved by 64-PSK and 64-QAM, respectively.

Fig. 3.13(c) shows the BER performance for different modulation schemes and carrier frequencies. We know that mm-wave band can operate in the frequency range of $(30, 300)$ GHz. In Fig. 3.13(c), we plot the results for the carrier frequency range $f_c = \{50, 70, \ldots, 110\}$ GHz. Note that we assume same value of path loss exponent $\gamma = 4$ in Fig. 3.13(c), however, atmospheric absorption due to oxygen is substantial at 60 GHz, when compared to that at other frequencies. Since, we assume $d = 25$ meters, signal attenuation due to oxygen absorption at 60 GHz (25 dB/km) is only 0.5 dB. Thus, same value of path loss exponent $\gamma = 4$ is used to plot the results in Fig. 3.13(c). As expected, the BER increases by increasing the carrier frequency, which implies that in order to achieve the same BER at higher carrier frequencies, the supportable distance between transmitter and receiver decreases. Fig. 3.13(c) shows that M-FSK offers smaller BER compared to M-PSK and M-QAM for the whole set of considered values of carrier frequency f_c. Particularly, for $f_c = 90$ GHz, 16-FSK achieves the BER $= 4.2 \times 10^{-4}$ which is 2.61 and 1.23 times smaller than that achieved by 16-PSK and 16-QAM, respectively. Similarly, 64-FSK
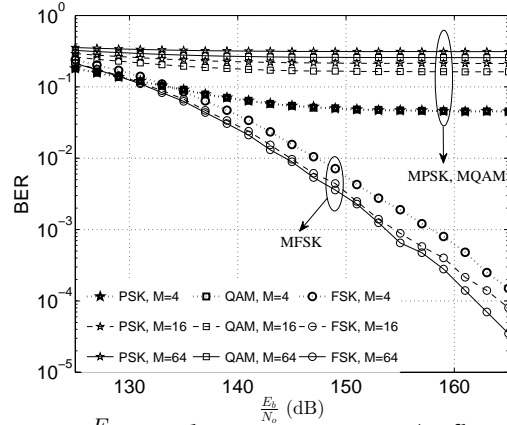
Figure 3.14: BER versus $\frac{E_b}{N_o}$ at the transmitter (reflects to $\frac{E_b}{N_o} = \{1, 6, \ldots, 41\}$ dB at the receiver) with all channel distortion and hardware impairments, e.g., phase noise variance $\sigma_{phn}^2 = 10^{-3}$, hardware distortion noise variance $\sigma_{nl}^2 = 0.2$, shadowing-standard deviation $\sigma_{shad}^2 = 9$ dB, path loss exponent $\gamma = 4$, and carrier frequency $f_c = 60$GHz.

achieves the BER $= 4 \times 10^{-4}$ which is 37.5 and 3.2 times smaller than that achieved by 64-PSK and 64-QAM, respectively.

3.3.2.4 Combined Effect of Hardware Impairments and Channel Distortions

Finally, Fig. 3.14 plots the most important results where we take into account the effect of all hardware impairments and the channel distortions. Specifically, we set the phase noise variance $\sigma_{phn}^2 = 10^{-3}$, hardware distortion noise variance $\sigma_{nl}^2 = 0.2$, shadowing-standard deviation $\sigma_{shad}^2 = 9$ dB, path loss exponent $\gamma = 4$, and carrier frequency $f_c = 60$GHz. Fig. 3.14 plots the BER for different modulation schemes against the range of values of $\frac{E_b}{N_o} = \{125, 130, \ldots, 165\}$ dB at the transmitter. *Again, note that if the signal attenuation of 124 dB caused by the transmission at carrier frequency $f_c = 60$ GHz and with path loss exponent $\gamma = 4$ (see calculations in Sec. 3.3.2), is ignored, $\frac{E_b}{N_o} = \{125, 130, \ldots, 165\}$ dB at the transmitter will translate to the range $\{1, 6, \ldots, 41\}$*

dB at the receiver, which is the range usually assumed in many papers. It can be observed from Fig. 3.14 that the combined effect of hardware impairments and channel distortions is very destructive on the application of M-PSK and M-QAM, i.e., the BER suffers from an error floor and is greater than 4×10^{-2} even at $\frac{E_b}{N_o} = 165$ dB. On the other hand, employing M-FSK achieves the BER $< 2 \times 10^{-3}$ at $\frac{E_b}{N_o} = 155$ dB. Specifically, by employing M-FSK, the BER does not suffer from an error floor under the considered wide range of $\frac{E_b}{N_o}$ and gets even lower than 2×10^{-4} at $\frac{E_b}{N_o} = 165$ dB. As expected, increasing the modulation size from $M = 4$ to $M = 16$ or 64 decreases the BER of M-FSK-based communication system. If we assume modulation size of $M = 4$, for which FSK requires only 4 times more bandwidth compared to that required by PSK or QAM, BER for FSK is about 315 times smaller than that for PSK or QAM at $\frac{E_b}{N_o} = 165$ dB. On the other hand, if we enjoy the ample bandwidth available for mm-wave communication, 64-FSK not only achieves more than 1300 times smaller BER but also delivers 4 times higher throughput (bits per second) when compared to 4-PSK or 4-QAM.

3.3.3   Conclusion

In this paper, we have demonstrated the application advantages of non-coherent FSK over other modulations schemes, e.g., PSK and QAM at 60 GHz band in the presence of hardware impairments and channel distortions. Through extensive system-level simulations, we have shown that non-coherent FSK, while enjoying vast bandwidth at mm-wave frequencies, combats the severe effect of pathloss, shadowing, amplifier non-linearity, and phase noise quite better than other modulations schemes such as PSK and QAM. This is mainly because the information in

non-coherent FSK is not affected by the phase distortion. Particularly, our extensive simulation results conclude the following.

- Considering the effect of hardware impairments (phase noise in Fig. 3.9 and amplifier non-linearity in Fig. 3.11) individually, our extensive simulations show that BER for 4-ary non-coherent FSK is about 100 times smaller as compared to the BER for 4-PSK or 4-QAM at transmitter $\frac{E_b}{N_o} = 155$ dB (receiver $\frac{E_b}{N_o} = 31$ dB). Similarly, considering the effect of channel distortions (shadowing in Fig. 3.13(a) and pathloss in Fig. 3.13(b)) individually, our extensive simulations show that BER for 16-ary non-coherent FSK is about 1.57 and 2.3 times, respectively, smaller as compared to the BER for 16-PSK or 16-QAM at transmitter $\frac{E_b}{N_o} = 150$ dB (receiver $\frac{E_b}{N_o} = 26$ dB).

- Considering the effect of all hardware and channel impairments together (Fig. 3.14), our extensive simulations show that BER for 4-ary non-coherent FSK is about 315 times smaller as compared to the BER for 4-PSK or 4-QAM at transmitter $\frac{E_b}{N_o} = 165$ dB (receiver $\frac{E_b}{N_o} = 41$ dB).

- Although there are several techniques to mitigate phase noise and nonlinear distortion for QAM and PSK, their application can significantly increase complexity of the transceiver, making them even less attractive than FSK. Exploration of these remedies and detailed comparisons are an area for future work.

This remarkable gain in terms of BER, combined with the low detection complexity of non-coherent FSK, makes it an attractive modulation for achieving multi Gbps wireless links at mm-wave frequencies.

3.4   Impact on Research and Quality of STEM

The impact of the acquired equipment on research and quality of STEM at CSUB is summarized in point-form below:

- *Research in the Area of Millimeter-Wave Communications:* The acquired equipment will make it possible for our students to carry out hands-on research in the new and evolving field of millimeter-wave communications. This new area of research will revolutionize wireless communications and networks. Thus, students with applied research experience in this field can more easily join the workforce or continue their education as masters or Ph.D. students.

- *Support a for Wide Range of Signaling Standards:* The previous testing and measurement equipment at CSUB did not allow for any form of signal analysis for the most recent standards used in defense, cellular, wireless connectivity, and aerospace applications. The acquired equipment has adds this capability to the Digital Signal Processing and Communications Laboratory at CSUB and allows the undergraduate students to focus on more sophisticated, applied, and practical research projects for the their senior design projects.

- *Better Access to Testing and Measurement Equipment:* As highlighted previously the Department of ECCS at CSUB has 250 majors in Electrical and Computer Engineering combined. However, the department was only equipped with a single signal generator and signal analyzer with a maximum operating frequency of 3 GHz. The new equipment has tripled the number of students that we are able to support for various labs and research projects.
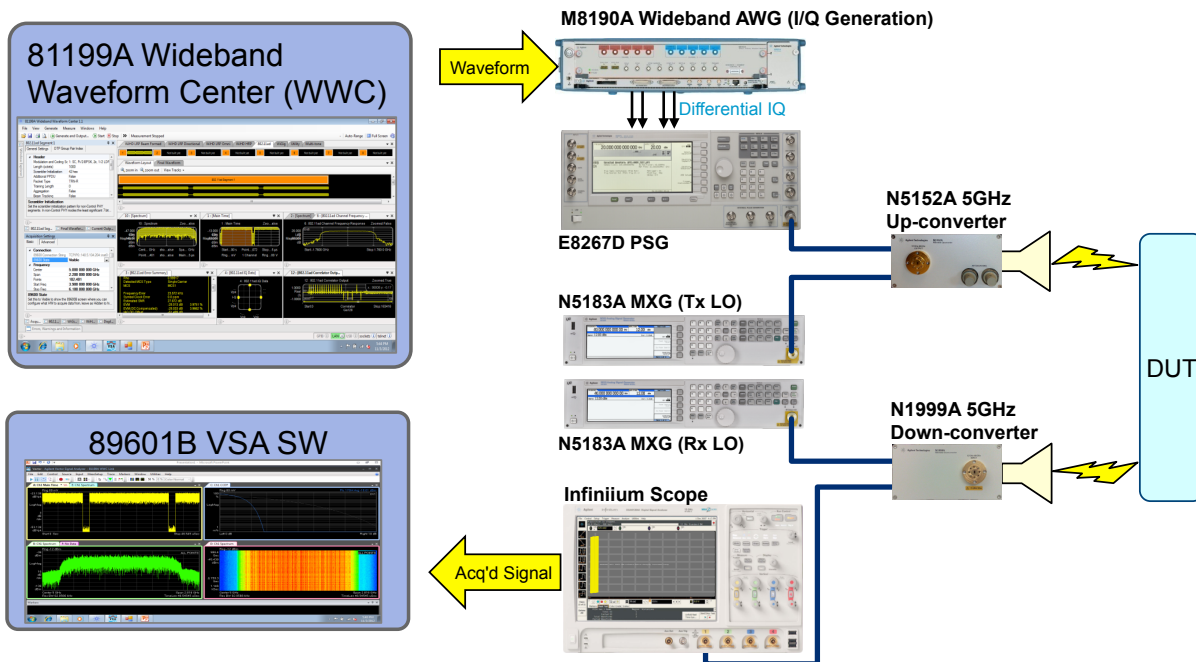
Figure 3.15: The mm-wave test bed available to PIs at Boise State University.

Note that due to the prohibitively high cost of the acquired equipment and lack of funding, we would not have been able to purchase such specialized equipment for research and training at CSUB. Hence, DoD's support has uniquely given us the opportunity to greatly improve the quality of research and student training in a wide range of courses and research projects. This improvement will also benefit the DoD by training the next generation of capable and outstanding engineers that can ensure the United States' continued dominance in military and defense research and development.

Fig. 3.15 illustrates the mm-wave test bed that is has been acquired as part of this funding. The test bed can support various modulations and standards such as IEEE 802.11ad, bandwidths of up to 12 GHz and frequencies in the 57 GHz to 66 GHz range. The test bed allows for various measurements such as: error vector
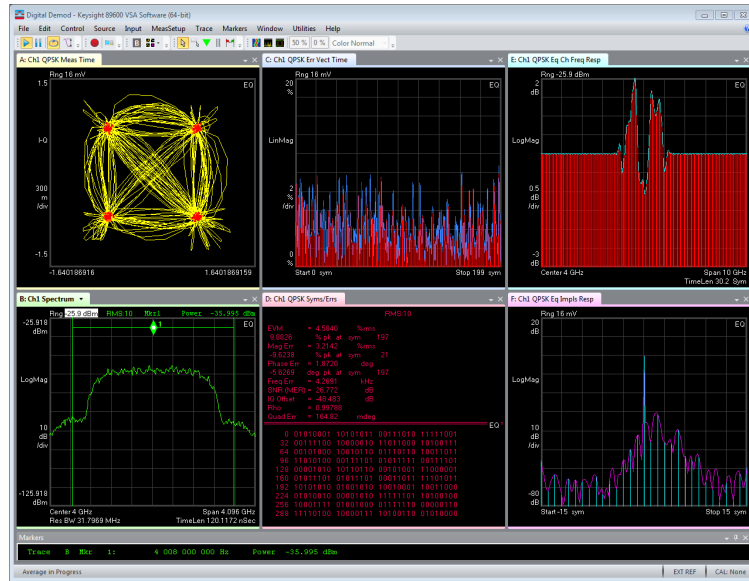
Figure 3.16: Phase noise measurement results via mm-wave test bed.

magnitude (EVM), channel power, channel flatness, occupied bandwidth, noise figure, and phase noise. *Fig. 3.16* demonstrates the phase noise measurements that we have obtained via the test bed in *Fig. 3.15*.

Appendix A

Resource Allocation Derivations

A.1   System Model

Here, we consider a downlink scenario in a single cell of a HetNet with a macro BS coupled with M relay BSs over the V- and E-band. N OFDM subcarriers are considered in each band for a two-hop transmission through the relay nodes. In order to avoid interference, no two users or relays are expected to utilize the same subcarrier. The relays are assumed to operate in half-duplex mode, i.e., they receive information in the first time slot and transmit in the second time slot. The bandwidth of each subcarrier is Δf. Multiple fixed relay nodes assist the BS in providing diversity and also extending the coverage in the cell consisting of K user or *destination* nodes, see Fig. 3.1. This is desirable at mm-wave frequencies due to significant pathloss and shadowing. In Fig. 3.1, $h_{SD_k}^{i,b}$, $h_{SR_m}^{i,b}$ and $h_{R_m D_k}^{j,b}$ represent the instantaneous channel fading parameters, where $k = \{1, ..., K\}$, $m = \{1, ..., M\}$, $i, j = \{1, ..., N\}$, and $b = \{f_1, f_2\}$. f_1 and f_2 refer to the 60 GHz and 70–80 GHz frequency bands. Here and considering $(.)_{cc'}^{a,b}$, the superscripts a and b denote the subcarrier and the selected frequency band, respectively, and subscripts c and c'

denote the transmitter and receiver of the communication link. Although we consider a HetNet structure, the interference from neighboring cells is assumed to be negligible since mm-wave systems take advantage of highly directional antennas that establish line-of-sight (LoS) links between the transmitter and receiver pairs [50]. This combined with the high free-space pathloss at mm-wave frequencies ensures that there is negligible inter cell interference in mm-wave HetNets [61].

It is assumed that *maximum ratio combining* (MRC) is used at the receiver's end, utilizing the spatial diversity in the proposed HetNet. Similar to [21,24,53,75], we assume a network operating on time division duplex. Hence, channel reciprocity is used to estimate all the channel parameters at the BS [21,24,39,53,75]. The BS is also assumed to perform the resource allocation in a centralized fashion and provide the information to the relays using the backhaul links interconnecting the relays to the whole network. This allows for simple hardware structures at the relays, which reduces their cost of deployment. Based on the channel conditions at both bands, the BS decides to either utilize the relays or transmit its information through the direct link. In order to send data over a given subcarrier pair (i, j) to a given user-relay pair (k, m), if the BS-to-relay and relay-to user link is favorable compared to the BS-to-user link, i.e.,

$$\alpha_{SR_m}^{i,b} > \alpha_{SD_k}^{i,b},$$

$$\alpha_{R_mD_k}^{j,b} > \alpha_{SD_k}^{i,b}, \tag{A.1}$$

then the relay link is used. Otherwise, the source to destination link is used. Here,

- $\alpha_{SR_m}^{i,b} = |h_{SR_m}^{i,b}|^2 / \sigma_{SR_m,i,b}^2$,

- $\alpha_{SD_k}^{i,b} = |h_{SD_k}^{i,b}|^2 / \sigma_{SD_k,i,b}^2$, and

- $\alpha_{R_m D_k}^{j,b} = |h_{R_m D_k}^{j,b}|^2 / \sigma_{R_m D_k,j,b}^2$ denote the normalized channel fading gains of the corresponding links over the mentioned subcarrier and the frequency band.

- $\sigma_{cc',a,b}^2$ denotes the additive noise power corresponding to the link between nodes c and c', over subcarrier a of the frequency band b.

Fig. 3.2 presents the transmission timing diagram for the proposed network. Based on (A.1) there are two modes of operation, *relay link mode* and the *direct link mode*. In the relay link mode, in the first time slot, the BS transmits data to both destination k and the relay m over subcarrier i. If the conditions in (A.1) are satisfied, the relay decodes and forwards the data to the destination k over subcarrier j in the second hop, which is not necessarily the same as subcarrier i in the first hop. This subcarrier pairing is performed based on sum-weighted-rate maximization criterion. In fact, the subcarriers in the first and second time slots can be either in the E- or V-band based on the channel conditions. Moreover, note that in the relay link mode, transmission takes place over both the direct and relay links. If the conditions in (A.1) are not satisfied, the relay does not forward its information to the destination, and the BS transmits data solely to the direct link and keeps silent in the second hop. This mode is referred to as the direct link mode.

It is notable that a particular relay node can serve more than one destination node and a destination node can receive data from different relays, as well. The proposed resource allocation is centralized at the BS and then the users and the relays are informed of the resource allocation parameters during the signaling process that proceeds data transmission, i.e., the hand-shaking stage. Different subcarriers may carry different types of services. Thus, to meet QoS requirements for each user, different weights are applied to different users in the system, which is

determined based on the priority of the requested service.

A.2 Resource Allocation

For a given user k that receives data through the BS and a relay m in the first and second time slots over subcarrier pair (i, j) in the frequency band b, the weighted normalized rate can be expressed as [24]:

$$R = \frac{1}{2} w_k \log_2(1 + \alpha_{k,m}^{(i,j),b} p_{k,m}^{(i,j),b}), \qquad \text{(bits/s/Hz)} \qquad \text{(A.2)}$$

where

- $p_{k,m}^{(i,j),b} = p_{k,m}^{S_{(i,j),b}} + p_{k,m}^{R_{(i,j),b}}$ is the aggregate power for subcarrier pair (i,j) of frequency band b,

- w_k represents the weight of QoS requirement for user k,

- $p_{k,m}^{S_{(i,j),b}}$ denotes the transmit power of the BS to a given user-relay pair (k, m), over subcarrier i that is paired with subcarrier j in the second hop,

- $p_{k,m}^{R_{(i,j),b}}$ shows the transmit power of the relay m to the user k, over subcarrier j that is paired with subcarrier i in the first hop, and

- $\alpha_{k,m}^{(i,j),b}$ is the equivalent channel gain for a given subcarrier pair(i,j) over band b, which is determined as [24]

$$\alpha_{k,m}^{(i,j),b} \triangleq \begin{cases} \dfrac{\alpha_{SR_m}^{i,b} \alpha_{R_m D_k}^{j,b}}{\alpha_{SR_m}^{i,b} + \alpha_{R_m D_k}^{j,b} - \alpha_{SD_k}^{i,b}}, & \text{relay link mode} \\ \alpha_{SD_k}^{i,b} & \text{direct link mode.} \end{cases} \qquad \text{(A.3)}$$

The aggregated power is obtained by solving the optimization problem. Then, using the equations below, the power of the BS and the relay nodes for a specific

user over the corresponding subcarrier are obtained, in the relay link mode.

$$p_{k,m}^{S_{(i,j),b}} \triangleq \frac{\alpha_{R_m D_k}^{j,b}}{\alpha_{SR_m}^{i,b} + \alpha_{R_m D_k}^{j,b} - \alpha_{SD_k}^{i,b}} p_{k,m}^{(i,j),b}, \tag{A.4}$$

$$p_{k,m}^{R_{(i,j),b}} \triangleq \frac{\alpha_{SR_m}^{i,b} - \alpha_{SD_k}^{i,b}}{\alpha_{SR_m}^{i,b} + \alpha_{R_m D_k}^{j,b} - \alpha_{SD_k}^{i,b}} p_{k,m}^{(i,j),b}. \tag{A.5}$$

In the direct link mode, the BS and the relay powers are given by $p_{k,m}^{S_{(i,j),b}} \triangleq p_{k,m}^{(i,j),b}$ and $p_{k,m}^{R_{(i,j),b}} \triangleq 0$, respectively.

The resource allocation problem under a minimum rate requirement for each user and a total power constraint can be formalized as

$$\max_{(\boldsymbol{p},\boldsymbol{\zeta})} \sum_{b,i,j,k,m} \frac{w_k}{2} \zeta_{k,m}^{(i,j),b} \log_2 \left(1 + \alpha_{k,m}^{(i,j),b} p_{k,m}^{(i,j),b}\right) \tag{A.6a}$$

subject to

$$\sum_b \sum_{m=1}^{M} \sum_{k=1}^{K} \sum_{j=1}^{N} \zeta_{k,m}^{(i,j),b} = 1, \quad \forall i, \tag{A.6b}$$

$$\sum_b \sum_{m=1}^{M} \sum_{k=1}^{K} \sum_{i=1}^{N} \zeta_{k,m}^{(i,j),b} = 1, \quad \forall j, \tag{A.6c}$$

$$\sum_{b,i,j,m} \frac{w_k}{2} \zeta_{k,m}^{(i,j),b} \log_2(1 + \alpha_{k,m}^{(i,j),b} p_{k,m}^{(i,j),b}) \geq R_{\min} \quad \forall k, \tag{A.6d}$$

$$\sum_{b,i,j,k,m} p_{k,m}^{(i,j),b} \leq P, \tag{A.6e}$$

$$p_{k,m}^{(i,j),b} \geq 0, \qquad \forall i, j, k, m, b, \tag{A.6f}$$

$$\zeta_{k,m}^{(i,j),b} \in \{0,1\}, \forall i, j, k, m, b. \tag{A.6g}$$

$\sum_{a,b,\ldots,z}$ is used to denote $\sum_a \sum_b \ldots \sum_z$ for better representation of the mathematical notations. Moreover, $\boldsymbol{p} \in \Re_+^{K \times M \times N \times N \times 2}$ and $\boldsymbol{\zeta}$ denote the sets of nonnegative real numbers with entries $p_{k,m}^{(i,j),b}$ and $\zeta_{k,m}^{(i,j),b}$. We define $\zeta_{k,m}^{(i,j),b}, \forall (i,j,k,m,b)$ as a binary factor in order to assist mathematical discussion of the resource allocation problem. $\zeta_{k,m}^{(i,j),b} = 1$ demonstrates that subcarrier pair (i,j) of the frequency band

45

b is allocated to the user-relay pair (k, m). Accordingly, (A.6b) and (A.6c) correspond to the constraints associated with the *exclusive* pairing of the subcarriers in the first and second time slots. In other words, in maximizing the sum-weighted-rate of the HetNet, there is only one subcarrier i in the first time slot that is paired with subcarrier j in the second time slot. Furthermore, (A.6e) represents the total power constraint for the networks. Practically, each user in the network also has a minimum rate requirement. We consider (A.6d) as a constraint in the resource allocation problem in order to provide each user with a minimum rate of R_{min}.

Since the optimization problem in (A.6) consists of a binary parameter $\zeta_{k,m}^{(i,j),b}$, solving it requires the application of integer programming, which has excessive computational complexity [7]. To make the problem tractable, we relax the integer factor as it can take real values within $[0, 1]$ and solve the Lagrangian dual problem instead of the primal one. After this relaxation, the objective function is a concave function in that it is a nonnegative weighted sum of concave functions in the form of $xlog(1 + y/x)$ [7]. It is worth mentioning that if the number of subcarriers is adequately large, the *duality gap* of a non-convex optimization problem reduces to *zero* [73]. After relaxing the constraint in (A.6g), the optimization problem in (A.6) can be rewritten as

$$\max_{(\boldsymbol{p}, \boldsymbol{\zeta})} \sum_{b,i,j,k,m} \frac{w_k}{2} \zeta_{k,m}^{(i,j),b} \log_2 \left(1 + \frac{\alpha_{k,m}^{(i,j),b} p_{k,m}^{(i,j),b}}{\zeta_{k,m}^{(i,j),b}}\right)$$

s.t. (A.6b), (A.6c), (A.6d), (A.6e), (A.6f)and

$$\zeta_{k,m}^{(i,j),b} \geq 0, \ \forall (b, i, j, k, m). \tag{A.7}$$

Subsequently, the dual problem is given by

$$\min_{\boldsymbol{\tau}, \boldsymbol{\delta}} D(\boldsymbol{\delta}, \boldsymbol{\tau}) = \min_{\boldsymbol{\tau}, \boldsymbol{\delta}} \max_{\boldsymbol{p}, \boldsymbol{\zeta}} \ L(\boldsymbol{p}, \boldsymbol{\zeta}, \boldsymbol{\delta}, \boldsymbol{\tau}) \tag{A.8}$$

$$\text{s.t.} \quad \text{(A.6b)} \quad \text{and} \quad \text{(A.6c)},$$

where the Lagrangian is given by

$$
L\left(p, \zeta, \tau, \delta\right) = \sum_{b,i,j,k,m} \frac{w_k}{2} \zeta_{k,m}^{(i,j),b} \log_2 \left(1 + \frac{\alpha_{k,m}^{(i,j),b} p_{k,m}^{(i,j),b}}{\zeta_{k,m}^{(i,j),b}} \right)
$$
$$
+ \sum_{k=1}^{K} \delta_k \Bigg(\sum_{b,i,j,m} \frac{w_k}{2} \zeta_{k,m}^{(i,j),b}
$$
$$
\times \log_2 \left(1 + \frac{\alpha_{k,m}^{(i,j),b} p_{k,m}^{(i,j),b}}{\zeta_{k,m}^{(i,j),b}} \right) - R_{\min} \Bigg)
$$
$$
+ \tau (P - \sum_{b,i,j,k,m} p_{k,m}^{(i,j),b}), \tag{A.9}
$$

where δ_k and τ are Lagrangian multipliers. Applying Kraush-Khan-Tucker (KKT) condition to the Lagrangian function, the expression for the optimal power allocation is derived as

$$
p^{*(i,j),b}_{k,m} = \zeta_{k,m}^{(i,j),b} \underbrace{\left[\frac{(1 + \delta_k)\, w_k}{2\tau} - \frac{1}{\alpha_{k,m}^{(i,j),b}} \right]^+}_{f_{k,m}^{(i,j),b}}, \tag{A.10}
$$

where $[x]^+$ indicates $\max(0, x)$.

In order to find the optimal value of the indicator $\zeta_{k,m}^{(i,j),b}$, we substitute (A.10) in the Lagrangian function and rewrite this function as

$$
L\left(p^*, \zeta, \tau, \delta\right) = \sum_{b,i,j,k,m} \zeta_{k,m}^{(i,j),b} Z_{k,m}^{(i,j),b} + C\left(\tau, \delta\right), \tag{A.11}
$$

$$
\tau^{l+1} = \tau^l - \varepsilon_1^l \left(P - \sum_{b,i,j,k,m} \zeta_{k,m}^{(i,j),b} f_{k,m}^{(i,j),b} \right), \tag{A.12}
$$

$$
(\delta_k)^{l+1} = (\delta_k)^l - \varepsilon_2^l \left(\sum_{b,i,j,m} \frac{w_k}{2} \zeta_{k,m}^{(i,j),b} \log_2(1 + \alpha_{k,m}^{(i,j),b} f_{k,m}^{(i,j),b}) - R_{\min} \right) \quad \forall k. \tag{A.13}
$$

where

$$Z_{k,m}^{(i,j),b} \triangleq \frac{(1+\delta_k)\,w_k}{2}\log_2(1 + \alpha_{k,m}^{(i,j),b} f_{k,m}^{(i,j),b}) - \tau f_{k,m}^{(i,j),b}, \qquad (A.14)$$

$$C\left(\tau, \delta\right) \triangleq \tau P - R_{\min}\sum_{k=1}^{K}\delta_k. \qquad (A.15)$$

Considering the fact that (A.15) is a constant value, the optimal value of $\zeta_{k,m}^{(i,j),b}$ is given by:

$$\zeta^{*}{}_{k,m}^{(i,j),b} = \begin{cases} 1 & \text{(k,m,i,j,b)=arg} \max_{k,m,i,j,b} Z_{k,m}^{(i,j),b} \\ 0 & \text{otherwise.} \end{cases} \qquad (A.16)$$

The Lagrangian multipliers are updated via

$$\tau^{l+1} = \tau^l - \varepsilon_1^l\left(P - \sum_{b,i,j,k,m}\zeta_{k,m}^{(i,j),b} f_{k,m}^{(i,j),b}\right), \qquad (A.17)$$

$$(\delta_k)^{l+1} = (\delta_k)^l - \varepsilon_2^l\left(\sum_{b,i,j,m}\frac{w_k}{2}\zeta_{k,m}^{(i,j),b}\log_2(1 + \alpha_{k,m}^{(i,j),b} f_{k,m}^{(i,j),b}) - R_{\min}\right) \qquad \forall k. \quad (A.18)$$

The iterative algorithm stops when

$$\frac{\left|\delta^{(l+1)} - \delta^{(l)}\right|}{\left|\delta^{(l+1)}\right|} < \varepsilon_\delta,$$

$$\frac{\left|\tau^{(l+1)} - \tau^{(l)}\right|}{\left|\tau^{(l+1)}\right|} < \varepsilon_\tau, \qquad (A.19)$$

where ε_δ and ε_τ are threshold selected to achieve a specific level accuracy in the obtained solutions.

Bibliography

[1] J. Alexovich and R. Gagliardi, "The effect of phase noise on noncoherent digital communications," vol. 38, no. 9, pp. 1539–1548, Sep. 1990.

[2] M. Ali, A. T. M. Sayem, and V. K. Kunda, "A reconfigurable stacked microstrip patch antenna for satellite and terrestrial links," *IEEE Trans. Veh. Technol.*, vol. 56, no. 2, pp. 426–435, Mar. 2007.

[3] J. Andrews, "Seven ways that hetnets are a cellular paradigm shift," *IEEE Commun. Mag.*, vol. 51, no. 3, pp. 136–144, Mar. 2012.

[4] O. E. Ayach, S. Rajagopal, S. Abu-Surra, Z. Pi, and R. Heath, "Spatially sparse precoding in millimeter wave MIMO systems," *IEEE Trans. Wireless Commun.*, vol. 13, no. 3, pp. 1499–1513, Mar. 2014.

[5] F. Bøhagen, P. Orten, and G. E. Øien, "Design of optimal high-rank line-of-sight MIMO channels," *IEEE Trans. Wireless Commun.*, vol. 6, no. 4, pp. 1420–1425, Apr. 2007.

[6] C. S. Bontu, D. D. Falconer, and L. Strawczynski, "Feasibility evaluation of high rate FSK data transmission and equalization for millimeter wave indoor radio," in *Proc. IEEE Int. Conf. Universal Personal Commu.*, Dec 1996, pp. 822–826.

[7] S. Boyd and L. Vandenberghe, *Convex optimization*. Cambridge university press, 2009.

[8] C. Caloz, T. Itoh, and A. Rennings, "CRLH metamaterial leaky-wave and resonant antennas," *IEEE Antennas Propagat. Mag.*, vol. 50, pp. 25–39, Oct. 2008.

[9] B. Cetiner, Z. Li, D. Rodrigo, and L. Jofre, "A new class of antenna array with a reconfigurable element factor," *IEEE Trans. Antennas Propagat.*, Apr. 2013.

[10] B. A. Cetiner, A. Grau, **H. Jafarkhani**, and F. D. Flaviis, "Multidisciplinary adaptive wireless communication systems: Reconfigurable MEMS integrated antennas & coding/decoding structures," in *Proc. IEEE Topical Conf. Wireless Commun. Tech.*, Jul. 2003.

[11] B. A. Cetiner, **H. Jafarkhani**, J.-Y. Qian, H. J. Yoo, A. Grau, and F. D. Flaviis, "Multifunctional reconfigurable MEMS integrated antennas for adaptive MIMO systems," *IEEE Commun. Mag.*, vol. 42, no. 12, pp. 62–71, Dec. 2004.

[12] J. Cheng, M. Hashiguchi, K. Iigusa, and T. Ohira, "Electronically steerable parasitic array radiator antenna for omni-and sector pattern forming applications to wireless ad hoc networks," in *Proc. IEE Microwaves, Antennas and Propagation*, vol. 150, Apr. 2003, pp. 203–208.

[13] A. Chorti and M. Brookes, "A spectral model for RF oscillators with power law phase noise," *IEEE Trans. Circuits Syst.*, vol. 53, no. 9, pp. 1989–1999, Sep. 2006.

[14] C. G. Christodoulou, Y. Tawk, S. A. Lane, and S. R. Erwin, "Reconfigurable antennas for wireless and space applications," *Proceed. of the IEEE*, vol. 100, no. 7, pp. 2250–2261, Mar. 2012.

[15] A. Demir, A. Mehrotra, and J. Roychowdhury, "Phase noise in oscillators: A unifying theory and numerical methods for characterization," *IEEE Trans. Circuits Syst.*, vol. 47, no. 5, p. 655674, May 2000.

[16] G. J. Foschini, "Layered space-time architecture for wireless communication in a fading environment when using multi-element antennas," *Bell labs technical journal*, vol. 1, pp. 41–59, Feb. 1996.

[17] J. Frigon, C. Caloz, and Y. Zhao, "Dynamic radiation pattern diversity (DRPD) MIMO using CRLH leaky-wave antennas," in *Proc. IEEE Radio and Wireless Symposium*, Jan. 2008, pp. 635–638.

[18] A. Ghosh, N. Mangalvedhe, R. Ratasuk, B. Mondal, M. Cudak, E. Visotsky, T. Thomas, J. Andrews, P. Xia, H. Jo, H. Dhillon, and T. Novlan, "Heterogeneous cellular networks: From theory to practice," *IEEE Commun. Mag.*, vol. 50, no. 6, pp. 54–64, Jun. 2012.

[19] A. Grau, M.-J. Lee, J. Romeu, **H. Jafarkhani**, L. Jofre, and F. D. Flaviis, "A multifunctional MEMS-reconfigurable pixel antenna for narrowband MIMO communications," in *Proc. IEEE Int. Symposium Antennas and Propagat.*, Jun. 2007.

[20] S. Hage-Ali, N. Tiercelin, P. Coquet, R. Sauleau, H. Fujita, V. Preobrazhensky, and P. Pernod, "A millimeter-wave microstrip antenna array on ultra-flexible micromachined polydimethylsiloxane (PDMS) polymer," *IEEE Antennas Wireless Propag. Lett.*, vol. 8, no. 8, pp. 1306–1309, 2009.

[21] Z. Hasan, E. Hossain, and V. K. Bhargava, "Resource allocation for multiuser OFDMA-based amplify-and-forward relay networks with selective relaying," in *Proc. IEEE Int. Conf. Commun. (ICC)*, 2011, pp. 1–6.

[22] M. Herdin, "A chunk based OFDM amplify-and-forward relaying scheme for 4G mobile radio systems," in *Proc. IEEE Int. Conf. Commun.*, vol. 10, Jun. 2006, pp. 4507–4512.

[23] C. Hoymann, W. Chen, J. Montojo, A. Golitschek, C. Koutsimanis, and X. Shen, "Relaying operation in 3GPP LTE: challenges and solutions," *IEEE Commun. Mag.*, vol. 50, no. 2, pp. 156–162, 2012.

[24] C.-N. Hsu, H.-J. Su, and P.-H. Lin, "Joint subcarrier pairing and power allocation for OFDM transmission with decode- and-forward relaying," *IEEE Trans. Signal Process.*, vol. 59, no. 1, pp. 399–414, Jan. 2011.

[25] K.-C. Huang and Z. Wang, *Millimeter Wave Communication Systems*. IEEE Series on Digital & Mobile Communication, 2011.

[26] ——, *Millimeter Wave Communication Systems*. John Wiley & Sons, 2011.

[27] G. Huff and J. Bernhard, "Integration of packaged RF MEMS switches with radiation pattern reconfigurable square spiral microstrip antennas," *IEEE Trans. Antennas Propagat.*, vol. 54, pp. 464–469, Feb. 2006.

[28] S. Jafar, "Blind interference alignment," *IEEE Selec. Topics in Signal process.*, vol. 6, no. 3, pp. 216–227, Jun. 2012.

[29] M. Khanzadi, R. Krishnan, D. Kuylenstierna, and T. Eriksson, "Oscillator phase noise and small-scale channel fading in higher frequency bands," in *Proc. IEEE Globecom*, Dec 2014, pp. 410–415.

[30] B. Li, Z. Zhou, H. Zhang, and A. Nallanathan, "Efficient beamforming training for 60-GHz millimeter-wave communications: A novel numerical optimization framework," *IEEE Trans. Veh. Technol.*, vol. 63, no. 2, pp. 703–717, Feb. 2014.

[31] S. Lim, C. Caloz, and T. Itoh, "Metamaterial-based electronically controlled transmission-line structure as a novel leaky-wave antenna with tunable radiation angle and beamwidth," *IEEE Trans. Micro. The. and Techniq.*, vol. 52, pp. 2678–2690, Dec. 2004.

[32] ——, "Beamwidth tuning in a composite right/left-handed (CRLN) leaky-wave antenna using non-uniformly biased varactors," in *Proc. European Micr. Conf.*, 2004, pp. 1077 – 1080.

[33] ——, "Metamaterial-based electronically controlled transmission-line structure as a novel leaky-wave antenna with tunable radiation angle and beamwidth," *IEEE Trans. Microw. Theory Tech.*, vol. 52, no. 12, pp. 2678–2690, Dec. 2004.

[34] ——, "Electronically scanned composite right/left handed microstrip leaky-wave antenna," *IEEE Micro. and Wireless Compon. Let.,*, vol. 14, pp. 277–279, Jun. 2004.

[35] D. Love, R. Heath, V. Lau, D. Gesbert, B. Rao, and M. Andrews, "An overview of limited feedback in wireless communication systems," *IEEE J. Sel. Areas Commun.*, vol. 26, no. 8, pp. 1341–1365, Oct. 2007.

[36] G. R. MacCartney, J. Zhang, S. Nie, and T. S. Rappapor, "Path loss models for 5G millimeter wave propagation channels in urban microcells," in *Proc. IEEE Globecom*, 2013.

[37] A. Martinez-Ros, J. Gomez-Tornero, and G. Goussetis, "Independent control of the leakage rate and pointing angle of a novel planar leaky-wave antenna," in *Proc. European Conf. Antennas and Propag.*, 2011, pp. 1919 – 1922.

[38] T. L. Marzetta, "Noncooperative cellular wireless with unlimited numbers of base station antennas," *IEEE Trans. Wireless Commun.*, vol. 11, no. 9, pp. 3590–3600, Nov. 2010.

[39] T. L. Marzetta and B. M. Hochwald, "Fast transfer of channel state information in wireless systems," *IEEE Trans. Signal Process.*, vol. 54, no. 4, pp. 1268–1278, Apr. 2006.

[40] M. Matthaiou, A. Papadogiannis, E. Bjornson, and M. Debbah, "Two-way relaying under the presence of relay transceiver hardware impairments," *IEEE Commun. Lett.*, vol. 17, no. 6, pp. 1136–1139, Jun. 2013.

[41] H. Mehrpouyan, S. D. Blostein, and T. Svensson, "A new distributed approach for achieving clock synchronization in heterogeneous networks," *in Proc. IEEE Global Commun. Conf. (Globecom)*, 2011.

[42] H. Mehrpouyan, M. Khanzadi, M. Matthaiou, A. Sayeed, R. Schober, and Y. Hua, "Improving bandwidth efficiency in e-band communication systems," *IEEE Commun. Mag.*, vol. 52, no. 3, pp. 121–128, March 2014.

[43] H. Mehrpouyan, A. Nasir, S. Blostein, T. Eriksson, G. Karagiannidis, and T. Svensson, "Joint estimation of channel and oscillator phase noise in MIMO systems," *IEEE Trans. Signal Processing*, vol. 60, no. 9, pp. 4790–4807, Sep. 2012.

[44] H. Mehrpouyan, M. Matthaiou, R. Wang, and G. K. Karagiannidis, "Hybrid millimeter-wave systems: A novel paradigm for HetNets," vol. 53, no. 1, pp. 216–221, Jan. 2014.

[45] A. A. Nasir, H. Mehrpouyan, R. Schober, and Y. Hua, "Phase noise in MIMO systems: Bayesian Cramer-Rao bounds and soft-input estimation," *IEEE Trans. Signal Processing*, vol. 61, no. 10, pp. 2675–2692, May 2013.

[46] Z. Pi and F. Khan, "An introduction to millimeter-wave mobile broadband systems," *IEEE Commun. Mag.*, vol. 49, no. 6, pp. 101–107, Jun. 2011.

[47] D. Piazza and K. Dandekar, "Reconfigurable antenna solution for MIMO-OFDM systems," *Electronics Letters*, vol. 42, pp. 446–447, Aug. 2006.

[48] D. Piazza, N. J. Kirsch, A. Forenza, R. W. Heath, and K. R. Dandekar, "Design and evaluation of a reconfigurable antenna array for MIMO systems," *IEEE Trans. Antennas Propagat.*, vol. 56, pp. 869–881, Mar. 2008.

[49] A. Porokhnyuk, T. Ueda, Y. Kado, and T. Itoh, "Nonreciprocal metamaterial for non-squinting leaky-wave antenna with enhanced beam steering," in *Proc. IEEE Antennas and Propag. Society Int. Symp.*, 2013, pp. 2289 – 2290.

[50] T. S. Rappaport, R. W. Heath, R. C. Daniels, and N. Murdock, *Millimeter-Wave Wireless Communications*. Prentice Hall, 2014.

[51] T. Rappaport, J. Murdock, and F. Gutierrez, "State of the art in 60-GHz integrated circuits and systems for wireless communications," *IEEE Commun. Mag.*, vol. 99, no. 8, pp. 1390–1436, Aug. 2011.

[52] C. Rodenbeck, M. yi Li, and K. Chang, "Circular-polarized reconfigurable grating antenna for low-cost millimeter-wave beam-steering," *IEEE Trans. Antennas Propagat.*, vol. 52, no. 10, pp. 2759–2764, Mar. 2004.

[53] G. A. S. Sidhu, F. Gao, and A. Nallanathan, "A joint resource allocation scheme for multi-relay aided uplink multi-user OFDMA system," in *Proc. Int. Conf. Wireless Commun. and Signal Process. (WCSP)*, 2010, pp. 1–6.

[54] B. Sklar, *Digital Communciations*. Prentice Hall, 2001.

[55] P. F. M. Smulders, "Statistical characterization of 60-ghz indoor radio channels," *IEEE Trans. Antennas Propag.*, vol. 57, no. 10, pp. 2820–2829, 2009.

[56] S. Sun and T. Rappaport, "Wideband mmwave channels: Implications for design and implementation of adaptive beam antennas," in *Proc. IEEE IMS*, 2014.

[57] A. L. Swindlehurst, E. Ayanoglu, P. Heydari, and F. Capolino, "Millimeter-wave massive MIMO: The next wireless revolution?" vol. 52, no. 9, pp. 56–62, Sep. 2014.

[58] A. Barbieri *et al.*, "LTE femtocells: System design and performance analysis," *IEEE J. Sel. Areas Commun.*, vol. 30, no. 3, pp. 586–594, Jun. 2012.

[59] A. Osseiran *et al.*, "Scenarios for 5G mobile and wireless communications: The vision of the METIS project," vol. 52, no. 5, pp. 26–35, May 2014.

[60] **H. Mehrpouyan**, M. R. Khanzadi, M. Matthaiou, A. M. Sayeed, R. Schober, and Y. Hua, "Improving bandwidth efficiency in E-band communication systems," *IEEE Commun. Mag.*, vol. 52, no. 3, pp. 121–128, Mar. 2014.

[61] **H. Mehrpouyan**, M. Matthaiou, R. Wang, G. K. Karagiannidis, and Y. Hua, "Hybrid millimeter-wave systems: A novel paradigm for HetNets," *IEEE Commun. Mag.*, vol. 53, no. 1, pp. 216–221, Jan. 2015.

[62] J. Wells, *Multi-Gigabit Microwave and Millimeter-Wave Wireless Communications*. Artech House., 2010.

[63] J. Zhang, *Femtocells: Technologies and Deployment*. John Wiley & Sons, Inc., 2010.

[64] S. Thompson *et al.*, "Constant envelope OFDM," vol. 56, no. 8, pp. 1300–1312, Aug. 2008.

[65] The METIS, "(mobile and wireless communications enablers for the twenty-twenty information society) 2020 project," Feb. 2013. [Online]. Available: http://www.metis2020.com/

[66] E. Topak, J. Hasch, C. Wagner, and T. Zwick, "A novel millimeter-wave dual-fed phased array for beam steering," *IEEE Trans. Microwave Theory Tech.*, vol. 61, no. 8, pp. 345–359, May 2013.

[67] E. Torkildson, U. Madhow, and M. Rodwell, "Indoor millimeter wave MIMO: Feasibility and performance," *IEEE Trans. Wireless Commun.*, vol. 10, no. 12, pp. 4150–4160, Dec. 2011.

[68] V. Vakilian, **H. Mehrpouyan**, and Y. Hua, "High-rate space coding for reconfigurable 2×2 millimeter-wave MIMO systems," in *Proc. IEEE Wireless Commun. Networking Conf.*, Mar. 2015, in press.

[69] V. Vakilian, **H. Mehrpouyan**, Y. Hua, and H. Jafarkhani, "High rate/low complexity space-time block codes for 2×2 reconfigurable MIMO systems," *submitted to IEEE Commun. Lett.*, 2015 http://arxiv.org/abs/1505.06729.

[70] ——, "High rate space-time codes for millimeter-wave systems with reconfigurable antennas," in *Proc. IEEE Global Commun. Conf.*, submitted 2015 http://arxiv.org/abs/1505.06466.

[71] W. Weedon, W. Payne, and G. Rebeiz, "MEMS-switched reconfigurable antennas," in *Proc. IEEE Int. Symposium Antennas and Propagat. Society*, vol. 3, Jul. 2001, pp. 654–657.

[72] J. Wells, *Multigigabit Microwave and Millimeter-Wave Wireless Communications*. Artech House, 2010.

[73] W. Yu and R. Lui, "Dual methods for nonconvex spectrum optimization of multicarrier systems," *IEEE Trans. Commun.*, vol. 54, no. 7, pp. 1310–1322, Jul. 2006.

[74] X. Zheng, Y. Xie, J. Li, and P. Stoica, "MIMO transmit beamforming under uniform elemental power constraint," *IEEE Trans. Signal Process.*, vol. 55, no. 11, pp. 5395–5406, Nov. 2007.

[75] N. Zhou, X. Zhu, Y. Huang, and H. Lin, "Optimal resource allocation for orthogonal frequency division multiplexing-based multi-destination relay systems," *IEEE Commun. Lett.*, vol. 5, no. 14, pp. 2075–2081, Sep. 2011.